(Received 25 April 2025, Accepted 4 February 2026, Scheduled 1 May 2026)

Acoustic Computation: From Effective Medium Theory to Biomedical Ultrasound Imaging

Erqian Dong[1], Sichao Qu[1,*], Xiaochuan Wu[1], Helios Y. Li[1], and Nicholas X. Fang[1,2,3,4,*]

[1]*Department of Mechanical Engineering, The University of Hong Kong, Hong Kong, China*
[2]*Materials Innovation Institute for Life Sciences and Energy (MILES), HKU-SIRI, Shenzhen, China*
[3]*Jockey-Club STEM Lab for Scalable and Sustainable Photonic Manufacturing, The University of Hong Kong, Hong Kong, China*
[4]*State Key Laboratory of Optical Quantum Materials, The University of Hong Kong, Hong Kong, China*

ABSTRACT: This paper reviews recent advances in acoustic computation and modeling, specifically bridging effective medium theory (EMT) and biomedical ultrasound imaging. To achieve this, we examine how EMT provides the physical foundation for wave-based imaging through homogenized parameters, focusing on image reconstruction across diverse systems ranging from single pulse-receivers to multi-input and multi-output (MIMO) tomography. Furthermore, we highlight cross-disciplinary insights from computational optics, such as the transport of intensity equation and ptychography, while addressing acoustic-specific challenges like aberration correction and wave interference. In light of these challenges, emerging solutions are discussed, including ultrasound matrix imaging (UMI) via transfer matrix methods, inverse-designed matching layers, and hardware-accelerated approaches like the Krimholtz-Leedom-Matthaei (KLM) electro-acoustic model for ultrafast imaging. Ultimately, by integrating physical understanding of effective media with advanced computational algorithms, these developments provide a robust framework for the future of high-resolution 3D ultrasonography and acoustic holography.

1. INTRODUCTION

Due to the exponential development of computer power in modern society following Moore's law [1, 2], the ancient discipline of acoustic calculation is experiencing a resurgence. The reason is simple: what was previously uncomputable can now be calculated, contributing to the advancement and deeper understanding of acoustic materials as well as related wave propagation. It is of note that the power law is similar to that of supercomputers, and commonly used graphics processing unit (GPU) technology, such as the NVIDIA GeForce series, can increase the number of operations per second for medical ultrasound and ultrafast imaging modalities. Another notable example is the discovery of acoustic metamaterials and their flourishing over the past two decades [3–6]. Meanwhile, owing to the increasingly mature advanced algorithms and software, the theoretical threshold of acoustic calculations has been lowered. Students, engineers, and more advanced scientists can simultaneously engage in the research and development of new algorithms, theories, and materials, accelerating the rapid progress of the field. Therefore, this study aims to examine the latest advancements in acoustic computing technology and address the challenges faced in the current context.

In addition to solving differential equations using grid-based numerical methods, including finite element methods and boundary element methods, there is another category of analytical or semi-analytical methods known as effective medium theories [7–11]. The importance of the former is self-evident, as it is a versatile and user-friendly choice. However, the latter requires a better understanding of physics to simplify specific problems and also provides higher efficiency. The theory of effective medium provides a fast response function (sometimes also considered as a physics-informed neural network), which can offer possibilities for the reverse design of high-performance metamaterials. At the same time, acoustic imaging is extremely vital in biomedical applications since the distribution of material components is usually unknown. Treating the system as a black box, the material spatial information of the system can be inferred completely or partially through different trial inputs. As shown in Fig. 1, the homogenization process of the acoustic effective medium is complementary to the imaging process. This can be seen from the relationship between spatial functions and time-frequency processing. The homogenization process encodes spatial information into the frequency domain. For example, the response of three different impedance barriers to sound waves, if we want to replace them with a piece of spatially uniform material, the overall equivalent parameters may exhibit dispersion (or local resonance) in the frequency domain. The imaging process (taking A-mode imaging as an example) is to invert the time-domain information into spatial information, and then obtain the approximate coordinates of the three materials. Time and frequency information can be collectively transformed into each other through the Fourier transform or its inverse version. In addition, the transformation (or the reciprocal transformation) into positional information is called the imaging process (or homogenization process). In this study, we review the

* Corresponding authors: Sichao Qu (qusichao@hku.hk); Nicholas X. Fang (nicxfang@hku.hk).

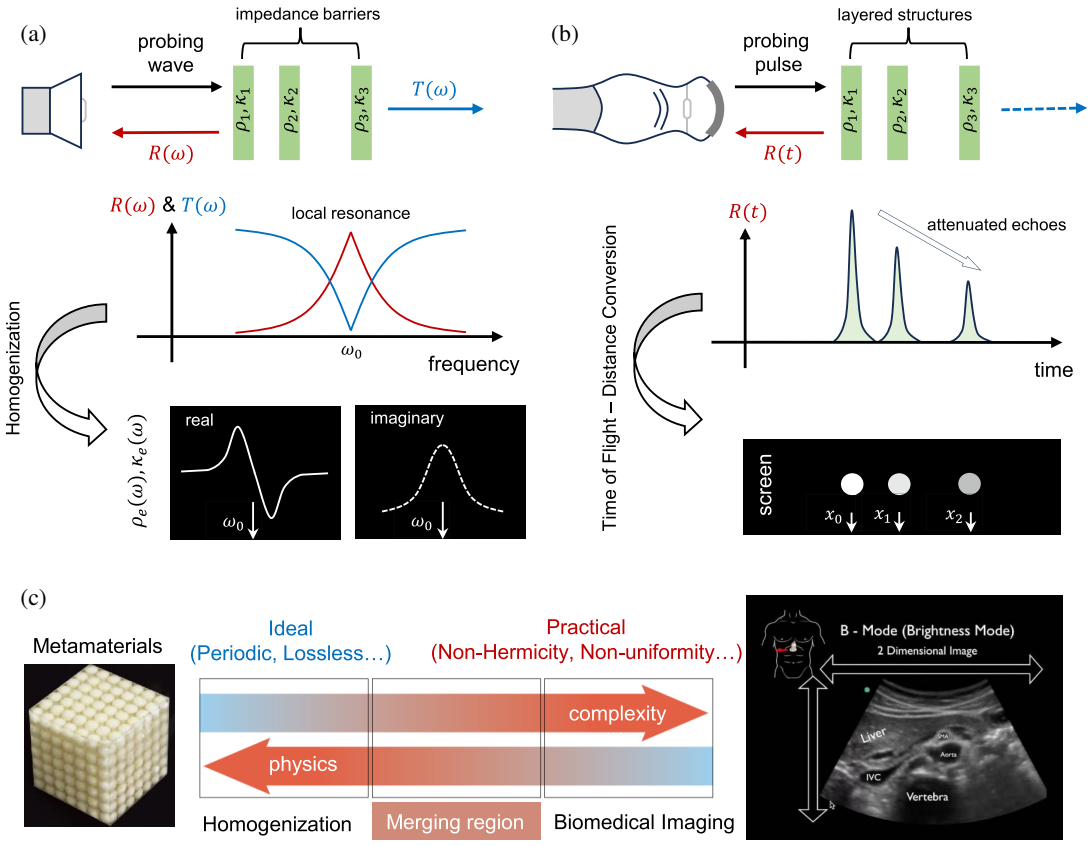

FIGURE 1. The complementarity between the effective medium theory and the imaging process. (a) The harmonic waves emitted by a signal source pass through three layers of impedance obstacles with a frequency sweep (steady states). By extracting the amplitude and phase of the reflected and transmitted spectra, we can accurately reconstruct the frequency response curve of the system (represented by effective density and effective bulk modulus). The spatial component information is transformed into frequency information. (b) The ultrasonic transducer emits a transient pulse, which is reflected by the same three layers of media. By extracting the flight time of the echoes, spatial information can be reconstructed. This one-dimensional process is known as A-mode imaging, forming the foundation for the more complex B-mode imaging process.

effective medium theories (homogenization) and biomedical imaging problems as well as their relations. The simplest toy model [e.g., Fig. 1] will be reviewed to help comprehend more complex concepts in an extended manner. We believe that a better understanding of the physical responses of effective media and materials will be beneficial for the advancement of imaging technology, and vice versa. In the domain of imaging technology, the use of simplified and approximate effective media is common, which can enhance efficiency and accuracy for specific medical ultrasound scenarios in the future. Both aspects are essential and mutually reinforcing in the development of acoustic calculations.

2. EFFECTIVE MEDIUM THEORY

Why do we need effective medium theories for ultrasound imaging? The answer can vary according to different perspectives. In acoustic calculations, these theories offer two key advantages: they significantly reduce computational complexity while accurately approximating the acoustic behavior of composite materials, and they provide insights into material resonance properties in the frequency domain, enabling practical modal analysis (the study of how structures respond to different frequencies). To introduce these concepts, let's explore a one-dimensional toy model that demonstrates the fundamental principles. This simplified approach will serve as a foundation for understanding more sophisticated applications in biomedical imaging. Acoustic properties are typically defined by mass density ρ and bulk modulus κ. If the scatterer includes a solid material, the extension of the mechanical equations should be considered (adding a parameter, such as Poisson's ratio ν or shear modulus G). However, in terms of acoustic calculations, the external domain is usually a fluid. Therefore, even if the scattering process involves solid mechanics, it will be homogenized using two parameters, including ρ_e and κ_e. Here, homogenization means considering the impact of excited solid mechanical modes (with longitudinal and/or shear motions) on the output longitudinal responses (due to the missing parameter of shear modulus in the environmental fluid). For special cases with higher-modes symmetry, the shear modulus should be reintroduced again [12]. Then, we will concisely introduce a few fundamental models and discuss the application conditions of acoustic homogenization.

2.1. Static Homogenization

The static effective medium refers to the situation under static limit or long wavelength conditions. When you are carrying a

bag of groceries from the store, your hand only feels the total weight, and cannot distinguish what components are inside the bag (without looking with your eyes). The same thing occurs in acoustics. Under the long wavelength limit [the left-side limit of the frequency response in Fig. 1(a)], the effective mass density and bulk modulus perceived by the sound waves also follow this principle. The concept of this static effective medium is similar to the series and parallel arrangement of resistors, that is, in the case of a direct current (corresponding to the static limits of sound/electromagnetic waves). Firstly, the bulk modulus can measure the stress response of a system when it is compressed or expanded under a strain. For a two-phase composite including a solid material in a fluid matrix, the static effective modulus is described by the famous Wood's formula [13]:

$$\frac{1}{\kappa_e} = \frac{f_1}{\kappa_1} + \frac{f_2}{\kappa_2}, \tag{1}$$

where the summation of volume fractions $f_1 + f_2 = 1$. The fluid matrix characterized by κ_1 and f_1 should be a topologically connected network. If Phase 1 is also a solid material, then Eq. (1) should be generalized by introducing the Poisson ratio ν_1 [14]. It should be noted that the applicability of Eq. (1) is limited, and a more general model should refer to the rule of mixtures [15], which can sometimes only give the upper and lower bounds of the composite modulus. Secondly, we review the calculation of the effective mass density. Throughout a long history, it was believed that the static limit density of sound waves is directly averaged over the volume: $\rho_e = f_1\rho_1 + f_2\rho_2$ [13], following the same definition as Eq. (1). But this is only true for acoustic waves when the composites are connected in series (layered structures). If composites are connected in parallel, which will allow relative motion between the different material phases, an exceptional case can lead to $\rho_e^{-1} = f_1\rho_1^{-1} + f_2\rho_2^{-1}$ (see an example of an acoustic hyperlens device in [16]). The generalized version of the effective mass density calculation was pioneered by Berryman [17], who proposed the following formula:

$$\frac{\rho_e - \rho_1}{(d-1)\rho_e + \rho_1} = f_2\frac{\rho_2 - \rho_1}{(d-1)\rho_2 + \rho_1}, \tag{2}$$

where d is the number of dimensions of the solid-fluid two-phase system. Eq. (1) and Eq. (2) were rigorously proven by taking a first-order approximation in the multiple scattering theory [9, 18] without the assumption of in-phase movement of all components. The interference of higher-order scattering channels will become significantly important when the volume fraction of the solid inclusion is large, i.e., the near-field interaction via evanescent waves should not be ignored. In this case, Eq. (2) should be corrected [19]. Moreover, this is also similar to the added mass in the calculation of the radiation impedance in the acoustic perforated plates [20, 21]. The spatial engineering of the static properties involves so-called gradient index/impedance materials [22–24].

2.2. Dynamic Homogenization

The discovery of locally resonant metamaterials [3, 4, 25] has propelled the revolutionary development of the theory of dynamic homogenization. Previously, most researchers believed that for phononic crystals, below the bandgap of Bragg scattering ($L \sim \lambda$), most frequency ranges could be effectively described using the static effective medium approximation. However, the emergence of local resonances ($L \ll \lambda$) with wavelengths several times larger, even hundreds of times larger than the unit size, has shattered this inherent understanding [26, 27]. Moreover, it is worth mentioning that these deep-subwavelength monopole and dipole resonances often lead to well-known phenomena, including negative density and negative modulus. The simplified mathematical forms for dipole [3] and monopole resonators [4] are as follows:

$$\rho_e = \rho_0 + \rho_m\frac{\omega^2}{\omega_d^2 - \omega^2}, \tag{3}$$

$$\kappa_e^{-1} = \kappa_0^{-1}\left(1 - \frac{\alpha_m}{\omega_m^2 - \omega^2}\right), \tag{4}$$

where ω_d and ω_m are the dipole and monopole resonance frequencies, respectively. The detailed derivations of the above Lorentzian forms are available in [10, 28] by locally calculating the eigenmodes and [29] with a focus on externally extracting the effective properties from a scattering matrix. Moreover, the importance of locally resonant metamaterials is also reflected in the fact that in the low-frequency region where traditional materials were incompetent, a wide range of dynamic properties can be controlled using relatively small metamaterials [27, 30]. These flexible and customizable features can play an important role in the field of imaging applications.

2.3. Extensions of Effective Medium Theories

As presented in Fig. 1(c), the ideal effective medium theory in material research may involve many potential assumptions, including periodicity, subwavelength approximation, non-dissipative approximation, spatial symmetry, isotropy, linearity, etc. When it comes to the understanding of complex media, including granular media and biomedical tissue, these assumptions may not hold true [31–34]. However, it does not mean that the effective medium theory is not useful. Furthermore, it still serves as a window to understand the propagation characteristics of waves. We emphasize that the emerging region between the fundamental physics and biomedical applications exhibits great potential for application opportunities. In practical complex acoustic systems (such as marine sediments, acoustic reverberation rooms, and biological tissues [35]), the original effective medium theory needs to be modified or modeled in a different way for wave propagation. Next, we will discuss some important extensions that may deepen our understanding in biomedical applications.

Non-Hermiticity. In wave physics, non-Hermiticity refers to the system not being able to return to its original state after time reversal, i.e., the broken time symmetry, which usually describes dissipative/gain systems [36]. Based on Fig. 1(b), it can be observed that the signal will experience attenuation during the imaging process, leading to a weakening of the received signal (reduced signal-to-noise ratio), which can explain why imaging deep tissues is challenging. In effective

medium theory, addressing dissipation can be challenging as it is often a fitting parameter, making it difficult to establish the dissipative mechanism from the ground up. However, there are still some commonly used viscous and non-viscous models for elastic media [37]. Furthermore, if we need to consider the frequency-dependent effects of the broadband, the Kramers-Kronig relations should be utilized [38, 39]. A successful example is that, by considering the correlation of frequencies, it is possible to recover as much imaging information as possible in dissipative media [40, 41]. *Non-uniformity*. The control of non-uniformity in waves is crucial, and rich physics is involved here. To some extent, imaging is also a process of analyzing non-uniformity information to assist in disease diagnosis. Important quantitative research has been established in the field of physics, inspiring a series of applied research. For example, gradient materials [22, 24, 42] can solve wideband impedance matching, focusing, and more; utilizing the extreme material properties of metamaterials can help waves pass through very hard obstacles [43] (such as skulls); using nonuniform metasurfaces can also increase imaging freedom, allowing a single detector to achieve good edge detection effects [44]. Moreover, overcoming and even utilizing non-uniformity to enhance the transmission of information in waves is a hot area with rich opportunities in the field of imaging. Next, we will further elaborate on how the non-Hermiticity and non-uniformity of materials affect and guide the design of ultrasound imaging systems. In ultrasound computation, these two correspond to the imaginary part of the refractive index and non-uniform density, which is equivalent to the variation of the scattering potential function in computational optical phase imaging.

3. WAVE PHYSICS ON COMPUTATIONAL IMAGING

Before delving into the specific computational imaging techniques, it is instructive to examine the well-established framework of optical wave physics. As a mature field, optical imaging has developed rigorous theories — such as coherence theory, phase retrieval, and iterative reconstruction methods — that provide both conceptual and mathematical foundations for understanding wave-matter interactions. These optical principles are not merely analogous but often directly transferable to the acoustic domain, particularly in the context of wave scattering, coherence, and inverse problems. In this section, we review key optical imaging modalities and their underlying theories, with an emphasis on how they have inspired and can be adapted to advance ultrasound imaging. Specifically, we will explore how the transport of intensity equation and ptychography offer alternative approaches to phase recovery and resolution enhancement, which address fundamental limitations in conventional delay-and-sum beamforming.

3.1. Optical Coherence Theory

Traditional optical imaging can be categorized into ghost imaging, coded aperture imaging, adaptive optical imaging, fluorescence imaging, polarization imaging, computerized tomography (CT), light field cameras, phase imaging, etc. The general framework of the optical coherence theory is well established based on the optical coherence theory and mutual coherence function $\Gamma(\mathbf{r}_1, \mathbf{r}_2, \tau) = \langle U^*(\mathbf{r}_1, t_1)U(\mathbf{r}_2, t_2)\rangle$, where the time difference $\tau \equiv t_2 - t_1$ and the angle brackets represent time averaging or equivalently for ergodic fields. $U(\mathbf{r}, t)$ is taken to be a scalar field, and the polarization effects are neglected. Furthermore, this kind of optical coherence theory can be readily extended to electromagnetics, as shown in the Wolf book [46]. In the classical theory of wave-focusing fields by partially coherent waves, the monochromatic and single-frequency spherical waves can be described as an expression based on the Huygens-Fresnel principle [47]:

$$U(\mathbf{r}, \omega) = -\frac{\mathrm{i}}{\lambda} \int_S U^{(0)}(\mathbf{r}', \omega) \frac{\mathrm{e}^{\mathrm{i}ks}}{s} \, \mathrm{d}S, \tag{5}$$

where $U^{(0)}(\mathbf{r}', \omega)$ is the field on the wavefront S that fills one specific aperture, $k = \omega/c = 2\pi/\lambda$ is the wavenumber associated with frequency ω corresponding to wavelength λ and light speed c. Here, $s = |\mathbf{r}' - \mathbf{r}|$ is the calculated distance from the observation point on the aperture surface $\mathbf{r}$ and integration point $\mathbf{r}'$. With the knowledge of wave field radiation patterns, Mie [48] laid the groundwork for the scattering of wave fields by a particulate medium, such as a colloidal suspension. The total field $U(\mathbf{r}, \omega)$ can be written as the sum of the incident field $U^{(i)}(\mathbf{r}, \omega)$ and scattered field $U^{(s)}(\mathbf{r}, \omega)$ as follows:

$$U(\mathbf{r}, \omega) = U^{(i)}(\mathbf{r}, \omega) + U^{(s)}(\mathbf{r}, \omega). \tag{6}$$

If we approximate the total field $U(\mathbf{r}, \omega)$ by the incident field $U^{(i)}(\mathbf{r}, \omega)$ in the side of the scattered integration $U^{(s)}(\mathbf{r}, \omega)$. The first-order Born approximation yields the expression:

$$U(\mathbf{r}, \omega) = U^{(i)}(\mathbf{r}, \omega) + \int_V F(\mathbf{r}', \omega) U^{(i)}(\mathbf{r}', \omega) G(\mathbf{r} - \mathbf{r}', \omega) \mathrm{d}^3 r', \tag{7}$$

where V is the volume occupied by the scatterer, and the scattering potential becomes $F(\mathbf{r}, \omega) = \frac{k^2}{4\pi}\left[n^2(\mathbf{r}, \omega) - 1\right]$ and $n(\mathbf{r}, \omega)$ represents the refractive index of the scatterers. The outgoing free-space Green's function associated with the Helmholtz operator is $G(\mathbf{r} - \mathbf{r}', \omega) = \frac{\mathrm{e}^{\mathrm{i}k|\mathbf{r}-\mathbf{r}'|}}{|\mathbf{r}-\mathbf{r}'|}$. Researchers have long noticed that the phase profile of the wave field has an unusual behavior in the near-zeros of amplitude, which is described by Sommerfeld in the textbook on optics. Later, the analogous dislocation in crystal structures by Nye and Berry [49] showed that the phase of the wave field contributes to the zeros of wave intensity. For example, the commonly described Young's double-pinhole interference experiment is illustrated in Fig. 2(a), where the zero of the interference pattern observed in the imaging screen corresponds to the zero surface in the three-dimensional space. If the number of the pinholes is increased to three or more, the zeros form from a line pattern to a hexagonal pattern, which is a typical feature of interference patterns containing a large number of these zero-intensity lines. For further analysis, these zero-intensity patterns are related to the phase singularities of coherent optics [50]. The concept of optical coherence,

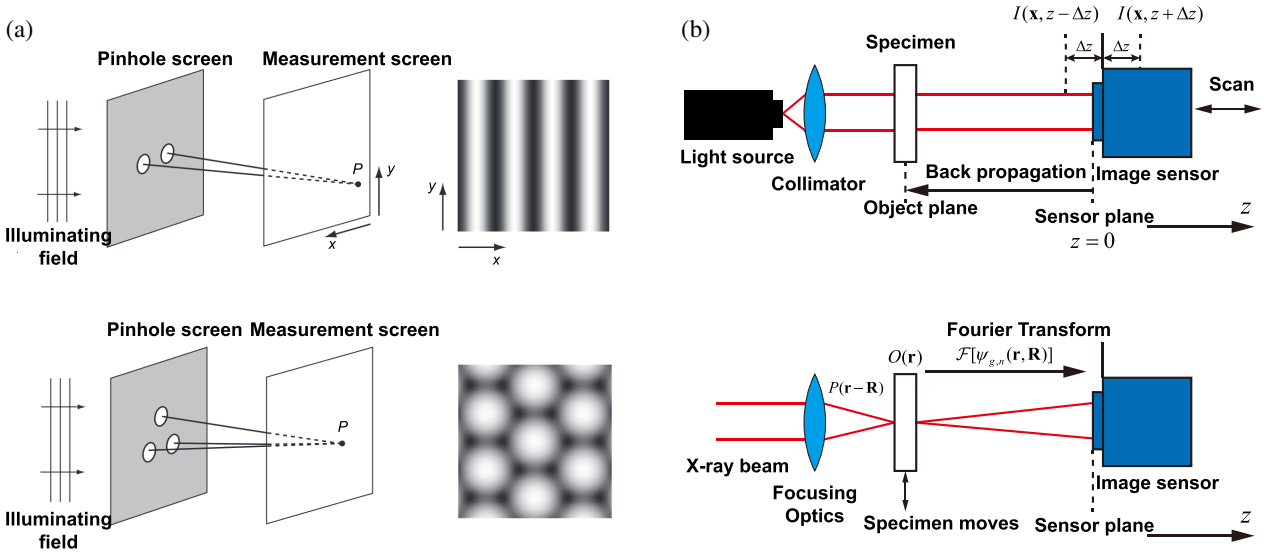

FIGURE 2. From Young's two-pinhole experiment to ultrasound tomography. (a) Illuminating fields modulated by two and three pinhole screen show the lateral and vertical resolution limit, respectively. The intensity of light observed on the measurement screen shows that zeros of the interference pattern are lines and a hexagonal pattern, respectively. (b) Schematic diagrams of TIE and ptychography, respectively. Panel (a) was adapted based on permission from [45].

encapsulated by the mutual coherence function, directly parallels the coherence properties of acoustic fields in medical ultrasound. In ultrasound imaging, the spatial coherence of backscattered signals determines the speckle statistics and image resolution, particularly in tissue environments where multiple scattering dominates. Understanding the coherence length and its dependence on source distribution — governed by the van Cittert-Zernike theorem — is essential for designing transducer arrays and beamforming strategies. Thus, the optical coherence theory serves as a critical starting point for analyzing and improving ultrasound imaging systems.

3.2. Transport of Intensity Equation

Distinguished from conventional intensity-based imaging, quantitative optical phase imaging techniques based on the Transport of Intensity Equation (TIE) [51] fully leverage the intensity and phase relationship of light during propagation to accurately solve for the phase. This enables the precise reconstruction of complex wave phase information using optical and electron microscopes. To recover the phase information, Teague et al. [52] derived the so-called transport-intensity equation (TIE):

$$-k\frac{\partial}{\partial z}I(\mathbf{x},z) = \nabla_\perp \cdot I(\mathbf{x},z)\nabla_\perp \phi(\mathbf{x},z), \tag{8}$$

where $\nabla_\perp$ is the transverse gradient operator. The above equation establishes a mathematical link between the axial derivative of the intensity and the spatial phase along the vertical direction. In other words, the axial derivative of the intensity is approximated by the finite differences as follows:

$$\frac{\partial}{\partial z}I(\mathbf{x},z) \approx \frac{I(\mathbf{x},z+\Delta z) - I(\mathbf{x},z-\Delta z)}{2\Delta z}, \tag{9}$$

where Δz is the defocus amount. In an optical system, the amount of defocus can be determined by moving the microscope to displace the detector along the axial intensity derivative direction. TIE-based phase imaging approaches are widely applied in biomedical imaging, such as quantitative phase microscopy in cell culture growth [53] and transmission electron microscopy [54]. Basically, TIE-based phase imaging considers a monochromatic, scalar field at the axial plane over the specimen between the white light illumination plane and the optical detector. Fundamentally, if there are two different polarized fields with the same intensities I_1 and I_2, the TIE technique can be readily extended to differential interference contrast (DIC) images, which can be regarded as a quantitative phase-imaging technology. Besides, the imaging process for TIE has been shown in the upper part of Fig. 2(b). The transport of intensity equation (TIE) provides a direct relationship between the axial intensity variation and the transverse phase gradient, enabling phase recovery without iterative algorithms. This principle is particularly attractive for ultrasound imaging, where phase information is often lost in conventional B-mode imaging due to envelope detection. By acquiring intensity maps at slightly different focal depths — analogous to the defocusing in optical microscopy — one could, in principle, retrieve the phase of the acoustic field. This approach offers a pathway to quantitative ultrasound imaging that accounts for phase aberrations and tissue-induced delays, moving beyond the simple geometric assumptions of delay-and-sum beamforming. Although acoustic implementations remain less mature, the success of TIE in optical microscopy strongly motivates its adaptation for ultrasound.

3.3. Optical Ptychography

In contrast to imaging methods that directly solve for the phase based on TIE, ptychographic imaging [55–57] based on scan-

ning phase recovery techniques provides greater freedom for reconstructing high-resolution sample information. The fundamental principle involves correlating and reconstructing phase information from multiple scanned images during the iterative reconstruction process. The characteristic of ptychographic imaging is based on translational invariance, which means that it requires regions of illumination must overlap with one another to facilitate the ptychographic translational invariance constraint. Rodenburg and Faulkner [58] proposed a phase retrieval algorithm for shifting illumination imaging, which considered the product of the specimen 2D complex transmission function $O(\mathbf{r})$ and the illumination function $P(\mathbf{r})$ by various distances $\mathbf{R}$. It assumes that only moving $P(\mathbf{r})$ with a fixed $O(\mathbf{r})$, the exit wave function $\psi(\mathbf{r})$ can be the product of $O(\mathbf{r})$ and $P(\mathbf{r}-\mathbf{R})$ as follows:

$$\psi(\mathbf{r},\mathbf{R}) = O(\mathbf{r})P(\mathbf{r}-\mathbf{R}). \tag{10}$$

The algorithm process can be found in Appendix A. The guessed object function can be updated by using the update function:

$$O_{g,n+1}(\mathbf{r}) = O_{g,n}(\mathbf{r}) + \frac{|P(\mathbf{r}-\mathbf{R})|}{|P_{\max}(\mathbf{r}-\mathbf{R})|} \frac{P^*(\mathbf{r}-\mathbf{R})\, E_{c,g,n}(\mathbf{r},\mathbf{R})}{\left(|P(\mathbf{r}-\mathbf{R})|^2+\alpha\right)}, \tag{11}$$

where $E_{c,g,n}(\mathbf{r},\mathbf{R}) = \beta(\psi_{c,n}(\mathbf{r},\mathbf{R}) - \psi_{g,n}(\mathbf{r},\mathbf{R}))$, and the parameters β and α can be chosen appropriately. $|P(\mathbf{r}-\mathbf{R})|$ is the maximum value of the amplitude function of $P(\mathbf{r})$ over the total diffraction region. As ptychographic imaging describes, the motion phase delay to form a motion-compensated image should essentially be the active reconstruction in ultrasound imaging, such as DAS coherent compounding [59]. The next step is to move to the next position $\mathbf{R}$, where the illumination overlaps with the previous region. The final step for ptychographic imaging is to repeat the above steps until the sum squared error (SSE) is sufficiently small:

$$\text{SSE} = \frac{(|\Psi(\mathbf{k},\mathbf{R})|^2 - |\Psi_{g,n}(\mathbf{k},\mathbf{R})|^2)^2}{N}, \tag{12}$$

where N is the number of pixels for the detector array elements. Based on the above initial ptychographic imaging algorithm shown in the lower part of Fig. 2(b), the phase retrieval with transverse translation diversity has been developed, which is based on a nonlinear optimization approach [60].

Ptychography's iterative reconstruction strategy — which synthesizes high-resolution images from overlapping, low-resolution measurements — offers a powerful paradigm for ultrasound imaging. In the acoustic domain, the equivalent concept appears in coherent plane-wave compounding, where multiple angled illuminations are coherently summed to improve image quality. However, unlike ptychography, conventional compounding does not explicitly solve for the complex object function through iterative updates. By adopting the ptychographic framework, ultrasound systems could potentially achieve super-resolution and aberration correction without requiring prior knowledge of the medium, particularly in scenarios where the illumination function (e.g., the transducer beam profile) is known, but the object is unknown. This cross-fertilization between optical ptychography and ultrasound beamforming represents a promising direction for future algorithmic development.

Conventional focused imaging (Fig. 7(d)) (128 focused beams, 4 focal depths) requires sequential transmissions and per-point delay-and-sum (DAS) beamforming. Its computational complexity scales as $O(N_e \cdot N_{\text{px}})$, where N_e is the number of array elements and N_{px} the number of image pixels, leading to a low frame rate ($\sim$25 fps) and high overall cost. This is analogous to confocal scanning microscopy, where point-by-point acquisition guarantees high resolution but at the expense of speed and heavy post-processing. Single-angle plane-wave imaging (one transmission) drastically reduces the number of firings, achieving $\sim$18000 fps. Its complexity is essentially that of a single DAS operation, i.e., $O(N_e \cdot N_{\text{px}})$ per frame, but with a constant factor much smaller than focused imaging. In optics, this corresponds to wide-field microscopy: one illumination yields an entire frame, trading off spatial resolution for speed.

Plane-wave compounding with 17 angles (Fig. 7(d)) ($\sim$1000 fps) coherently sums 17 plane-wave responses. The computational cost increases linearly with the number of angles, i.e., $O(17 \cdot N_e \cdot N_{\text{px}})$. While this offers a substantial improvement in image quality (comparable to conventional focused imaging), the required memory and summation steps grow proportionally. This scenario is akin to Fourier ptychography or structured illumination microscopy with a small number of illumination directions: the synthetic aperture is partially filled, providing a balanced compromise between resolution and throughput. 40-angle compounding ($\sim$350 fps) further improves the signal-to-noise ratio and resolution at the cost of a nearly 2.4$\times$ higher computational load compared to the 17-angle case. Its complexity $O(40 \cdot N_e \cdot N_{\text{px}})$ makes it less suitable for real-time three-dimensional imaging but remains feasible on modern GPU architectures.

From an algorithmic efficiency perspective, all DAS-based methods share a common structure that can be expressed as a sparse matrix-vector product (SpMV), as noted in Section 5.1. The sparsity of the DAS matrix enables GPU acceleration, yet the scaling with the number of compounded angles is linear. In contrast, optical ptychography (Section 3.3) employs an iterative update scheme (Eq. (11)) whose per-iteration complexity is dominated by fast Fourier transforms (FFTs), typically $O(N_{\text{px}} \log N_{\text{px}})$. While ptychography requires multiple iterations and overlapping measurements, its asymptotic scaling can be more favorable for high-resolution reconstruction than brute-force angle compounding. The key link is that both plane-wave compounding and ptychography exploit multiple illuminations (angles or translated probes) to surpass the resolution limit of a single shot. However, ultrasound compounding performs a linear coherent summation, whereas ptychography solves a nonlinear phase retrieval problem, enabling super-resolution without explicit knowledge of the object's support. This cross-disciplinary insight suggests that adopting pty-

chographic iterative engines for ultrasound — replacing linear DAS compounding with an optimization-based reconstruction — could potentially reduce the number of required angles (thus lowering computational cost) while maintaining or even enhancing image quality, especially in the presence of aberrations. Thus, the choice among the four modalities represents a clear trade-off among speed, image fidelity, and computational resources, directly analogous to the trade-offs between wide-field, structured illumination, and ptychographic or holographic methods in optical imaging.

While coherence and iterative retrieval offer a robust mathematical bridge for cross-disciplinary transfer, localized modifications are essential to account for fundamental physical divergences. First, although both fields exhibit vectorial properties, their manifestations differ: optical polarization is frequently simplified as a transverse scalar field, whereas acoustic waves in biological tissues involve complex coupling between longitudinal and shear mechanical modes. This requires integrating parameters such as the shear modulus and Poisson's ratio, which are typically absent in optical models. Second, while both domains experience absorption and dispersion, these effects are more pronounced in acoustics and follow distinct physical laws. Ultrasound is subject to intense, frequency-dependent attenuation and non-linear dispersion within human tissue, necessitating corrections — such as the Kramers-Kronig relations — to ensure signal alignment. Finally, detection mechanisms impose unique constraints; whereas optical sensors capture intensity patterns, acoustic systems modeled via the KLM network are limited by the transducer's emission response and real-time data processing rates. Recognizing these non-uniformities is critical for successfully adapting optical TIE or ptychography into reliable tools for quantitative ultrasound.

3.4. Ultrasound Imaging

Due to the well-developed optical wave imaging theory, ultrasound imaging exhibits exceptional adaptability in transferring similar mechanisms to itself. As initial attempts, considering the limited power of computer resources, it is not surprising that ultrasound tomography was realized based on the simplified acoustic wave equation with constant density values as follows:

$$\nabla^2 p(\mathbf{r}) + k^2(\mathbf{r}) p(\mathbf{r}) = 0. \tag{13}$$

If the plane wave solution $p = p_0 \exp(-\mathrm{i}k_0\tau(\mathbf{r}))$ is considered and rewritten into the wave equation under the high-frequency approximation $\lambda_0 \to 0$, the eikonal equation can be written as:

$$|\nabla\tau(\mathbf{r}, c)|^2 = n^2(\mathbf{r}), \tag{14}$$

where $n(\mathbf{r}) = c_0/c(\mathbf{r})$ is the refractive index, and $\tau(\mathbf{r})$ is the acoustic wavefront. In the seminal work on optical imaging back in 1969, Emil Wolf [61] proposed a method to reconstruct three-dimensional distributions of the refractive index using the scattered field $U^{(s)}(\mathbf{r}, \omega)$. In addition, for the case of constant-density acoustic wave equation, it can also be written as the combination of the incident acoustic pressure field and scattered field based on Wolf, invoking the first-order Born approximation as:

$$p(\mathbf{r}, \omega) = p^{(i)}(\mathbf{r}, \omega) + \int_V O(\mathbf{r}', \omega) p^{(i)}(\mathbf{r}', \omega) G(\mathbf{r} - \mathbf{r}', \omega) \mathrm{d}^3 r', \tag{15}$$

where $O(k, \mathbf{r}) = (k^2 - k_0^2)$ is the scattering potential function, and $G(\mathbf{r} - \mathbf{r}', \omega) = \frac{\mathrm{i}}{4} H_0^{(1)}(k_0|\mathbf{r} - \mathbf{r}'|)$ represents the Green's function based on the zero-order Hankel function of the first kind. The form of the first-order Born approximation is similar to Eq. (7). As expected, the simplifications above turn into limitations in extending ultrasound emission mechanisms, namely, the assumption of constant density value, linear wave generation and propagation, and high-frequency approximation. In a counterexample, photoacoustic imaging shows more superiority over conventional ultrasound imaging in higher imaging resolution and the introduction of more biomedical information containing anatomical, molecular, and radical data. The photoacoustic effect refers to a comprehensive response of materials receiving optical excitation. With photon energy deposition, the following heat generation, changes in optical, thermal, and mechanical properties, and then thermal expansion, eventually emission of the ultrasound signal, are closely interrelated. It is not hard to notice that this violates the limitations of applying the above eikonal equation given the nonlinear processes. Although photoacoustic imaging was observed for a long time and developed as a fastest-growing technique, its full application strongly depends on ultrasound detection and processing. Conventional photoacoustic microscopy neglected the nonlinear processes above and embraced the well-developed linearized ultrasound theoretical basis. Photon energy absorption, thermal diffusion, and then thermal expansion are linearly described within the restriction of thermal confinement and stress confinement, $\tau_p \ll \tau_{th}$ and $\tau_p \ll \tau_s$, that is, the laser pulse width is much shorter than heat diffusion time and stress response time, respectively. Under the above simplifications and plane wave condition in a uniform medium, thermal expansion induced pressure rise follows ultrasound-like acoustic wave equation solution [62]:

$$p_0(z, t) = \Gamma \mu_a F_0 \mathrm{e}^{-\mu_0 z}, \tag{16}$$

where Γ refers to the Grüneisen coefficient representing the thermal properties; μ_a is the optical absorption coefficient, which denotes the simplified optical properties; F_0 refers to the incident laser fluence; and μ_0 is the acoustic attenuation coefficient. Nevertheless, the change in the excitation of ultrasound offers exclusive functional potential in photoacoustic imaging, such as neurovascular imaging [63, 64], blood flow and lymphatic imaging [65], oxygen saturation imaging [66], and tumor tissue imaging enhanced by contrast agents [67]. Based on the precise measurement of the scattering potential function and refractive index, medical ultrasound tomography technology can separate the scattered field information from the total field. Further algorithms are developed to reconstruct the object by frequency hopping reconstruction or tomographic forward and backward integration, which will be discussed in the next part.

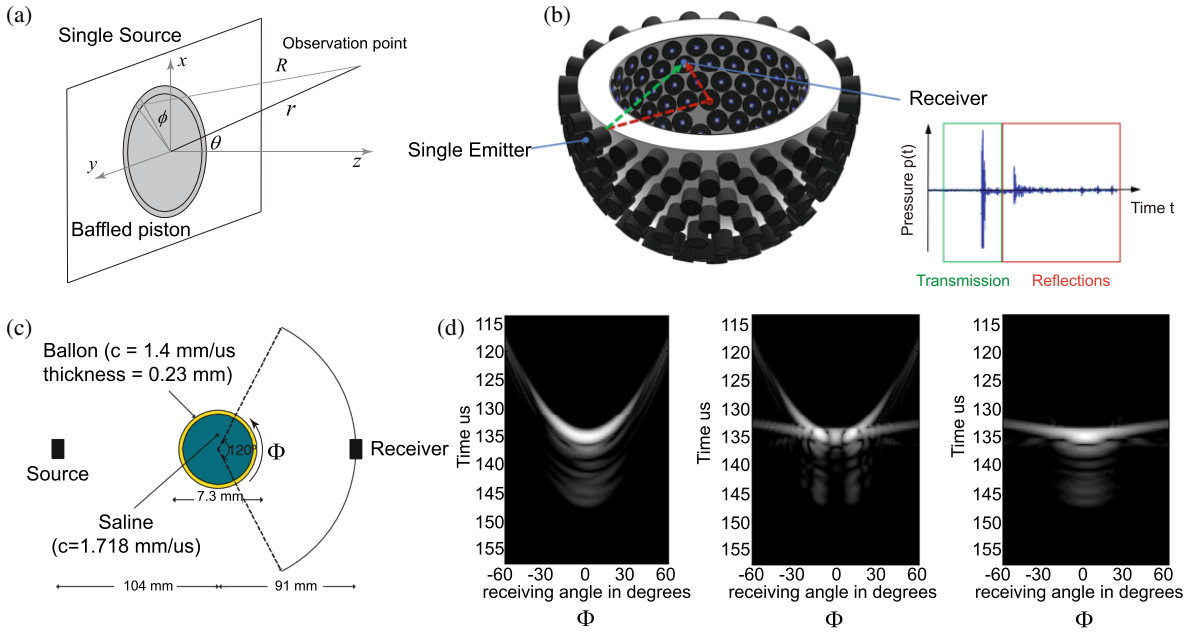

FIGURE 3. From single ultrasonic pulse-receiver (PR) imaging to multi-input and multi-output (MIMO) system. (a) Plane piston radiation source with infinite large barrier in free space corresponds to a two-dimensional axis symmetry case. Phased array sources with a specific time delay line in 2D case for transmit beam-formation with a certain incident angle θ. (b) From acoustic ray path to the multi-input and multi-output (MIMO) ultrasound tomography (USCT) system. (c) Scattering determination by given saline inside of a balloon and thickness evaluation by rotating amplitude imaging. (d) exhibits the forward propagating wave, total field, and scattering field, respectively. Panels (b) were adapted based on permission from [68]. Panel (c) was adapted based on permission from [69]. Panel (d) was adapted based on permission from [70].

4. MEDICAL ULTRASOUND TOMOGRAPHY

4.1. X-Ray Tomography to Ultrasound USCT

Similar to the wave focusing fields by a partially coherent light field, the acoustic field at the measurement point is expressed in terms of the velocity potential $\phi(x, y, z)$ by the Rayleigh integral:

$$\phi(x, y, z) = \int_S \frac{v_0 \mathrm{e}^{\mathrm{j}(\omega t - kr)}}{2\pi r} \mathrm{d}S. \tag{17}$$

The coordinate system is shown in Fig. 3(a), and v_0 is the amplitude of the particle velocity. This integral is simply an expression of Huygens' principle that the acoustic field at a measured point (x, y, z) can be the sum of all the spherical radiating points. If considering that there is one circular plane piston [71–74] in a rigid baffle, the full field can be obtained by the following formula based on Rayleigh's formula:

$$p = \frac{\mathrm{i}\omega\rho_0}{2\pi} \mathrm{e}^{\mathrm{i}\omega t} \int_S \frac{v \mathrm{e}^{-\mathrm{i}kR}}{R} \mathrm{d}S, \tag{18}$$

where R is the distance from the plane piston source to the observation point, and ϕ, θ are the two azimuthal angles, respectively. From the perspective of a single plane piston transducer, researchers have integrated ultrasound transducer arrays, where the point scatterer or object in water is surrounded by arrays with both ultrasound transmission and reception abilities. Before the array system became the most popular technology, an ultrasound camera under transmission mode had been used for water tank measuring [75]. In addition, some new algorithms can also be integrated into multi-array systems to make full use of the unfocused plane piston radiation sources with different transmission and reception angles that make the objects to be imaged as much as possible. As shown in Fig. 3(b), when the plane piston source dimension is smaller than the wavelength, the approximate pulsed spherical wavefront can be generated from a single emitter, and all other transducers receive the resulting field. In the right panel of Fig. 3(b), an A-scan is depicted for the indicated emitter-receiver combination as a pressure signal versus time. To analyze the different time-domain signals, it can be divided into two types of A-scan signals: including transmission signals (green signal) and reflection signals (red signal). The transmission signals are from the fastest path (or the shortest path) from a single emitter to a specific receiver, and the reflection path is scattered, as indicated by the dashed red line. Other multiple scattered signals in the reflections represent other paths and interactions of scatterers inside background water. The first publication for utilizing USCT can be traced back to the 1970s by Schomberg [76]. Recently, X-ray-induced acoustic tomography has also been developed by using radiation-induced acoustic waves for three-dimensional (3D) X-ray imaging. Achieving resolutions of $0.4\,\mathrm{mm}$ in the XZ plane and $3.5\,\mathrm{mm}$ in the XY plane at a depth of $16\,\mathrm{mm}$ [77], which is benefited from the absorption of X-ray energy by the soft tissue to produce spatial pressure changes. X-ray tomography can determine the Hounsfield unit (HU) scale, which is a linear transformation of the original attenuation coefficient into two different HU values, including the radiodensity of distilled water and air at standard pressure

and temperature (STP). The HU values for distilled water and air are 0 and 1000, respectively, and for the given linear attenuation coefficient μ_{material} in a certain voxel, the corresponding HU value is therefore given by [78]:

$$HU_{\text{material}} = 1000 \times \frac{\mu_{\text{material}} - \mu_{\text{water}}}{\mu_{\text{water}}}, \tag{19}$$

where μ_{water} and μ_{material} are the relative linear attenuation coefficients of water and the reconstructed matrix values in the CT image, respectively. It can be seen that when $\mu_{\text{material}} = \mu_{\text{water}}$, $HU_{\text{material}} = 0$ and $HU_{\text{material}} = -1000$ when $\mu_{\text{material}} = 0$. From the variation of HU values, except for the water and air, other types of the materials, such as contrast-enhanced blood and bone, have a relatively high effective atomic number, since the function of the phonon energy of materials is a nonlinear relationship with the linear attenuation coefficient in water and air. Analogous to reconstructive X-ray tomography, USCT can determine the spatial distribution by the refractive index or attenuation coefficient from an object illuminated by ultrasound beams instead of X-rays. For the simplest case, we assume that the speed of sound inside the medium is uniform (c). The two-way travel times of the wavefronts from the transducer coordinates x_i to the scatterer coordinates. The reconstruction methods of USCT are based on the inhomogeneous acoustic Helmholtz equation. According to the physical definitions of different parameters to describe USCT, the wave modeling can be further simplified as diffraction, refraction, scattering, and absorption, respectively. The wave-based reconstruction methods can be grouped into two categories: Full-wave Tomography, which uses the full information of the diffraction field, and Paraxial and Diffraction Tomography, which use an approximate method for reconstruction. One of the attenuation mapping methods by the attenuation coefficient of the objects was proposed by Carson and Oughton [79], and the refractive index mapping by time-of-flight measurements was proposed by Glover and Sharp [80] in 1977. In the conventional approach, it is assumed that each pulse generated from the transmit transducers travels along a straight line and arrives at the receiver positions. Under this assumption, the refractive index $n = v_0/v$, where v_0 is the sound velocity in water, and spatial varying sound velocity v indicates the refractive index from the object. According to eikonal Eq. (14), the conventional reconstruction algorithm can be described as follows:

$$\int_{r_{kl}} n \mathrm{d}s = v_0 T_{kl} \quad k = 1, \ldots, K;\ l = 1, \ldots, L. \tag{20}$$

where r_{kl} means the straight line between the emitter and receiver at position (θ_k, η_l). Contrary to the traditional pulse-echo ultrasonography, the imaged objects are surrounded by a fixed transducer array and in such a way that both transmission and reflection images of the speed of sound and attenuation distribution can be reconstructed. The transducer arrays with optimized spatial distributions and dimensions for generating spherical waves can overcome the challenges posed by the highly spatially variable and anisotropic properties by B-scan reflected sonography. If considering that the absorption is assumed to be smaller over the distance of one wavelength, the refractive index can be written as:

$$\eta(x) \approx \frac{c_0}{c(x)} + \mathrm{i}\,\frac{\mu(x)}{k_0}, \tag{21}$$

where μ is the spatial and frequency-dependent absorption coefficient, and attenuation coefficient α is often calculated instead of the absorption. Following the Born approximation as shown in Eq. (7), the scattered field [81] can be simplified to:

$$\hat{p}^{sct}(\mathbf{x}) = \omega^2 \int_{\mathbf{x}' \in \mathbb{D}} \hat{G}(\mathbf{x} - \mathbf{x}') \hat{p}^{inc}(\mathbf{x}') \times \chi(\mathbf{x}') \mathrm{d}A(\mathbf{x}'), \tag{22}$$

where the total pressure field $\hat{p}(\mathbf{x}')$ can be approximated by the incident ultrasound field $\hat{p}^{inc}(\mathbf{x}')$. Moreover, it should be noticed that the Born approximation assumes that the object to be reconstructed is small, and the scattering effect is weakly distinguishable from the background medium, and the Rytov approximation constrains the maximum object contrast. The above-mentioned diffraction tomography is based on a full-wave simulation method and can also be classified into several diffraction tomography approximations, such as Born or the Rytov approximation, in the first order of the wave equation [82]. Some of the low-frequency diffraction tomography studies in 2D imaging systems can be found from Greenleaf et al. [83], André et al. [84], Chenevert et al. [85], and Simonetti et al. [86]. By invoking the first-order Born approximation. As shown in Eq. (22), the total acoustic field $p(\mathbf{r}, k)$ can be approximately equal to the incident field $p(\mathbf{r}, k) \approx p^{inc,k_b}(\mathbf{r}) = p(\mathbf{r}, k_b)$. The combination of the incident acoustic field and scattered field can be approximated as the inverse solver equation:

$$p(\mathbf{r}, k) - p(\mathbf{r}, k_b) \approx \int \mathrm{d}\mathbf{r}' \left[k^2(\mathbf{r}') - k_b^2(\mathbf{r}')\right] p(\mathbf{r}', k_b) G_b(\mathbf{r}, \mathbf{r}'). \tag{23}$$

Since the unknown wave number function $k^2(\mathbf{r}') - k_b^2(\mathbf{r}')$ has the unknown term $k^2(\mathbf{r}')$ and a set of measured acoustic fields $p(\mathbf{r}, k)$, the initial guessed background pressure field $p(\mathbf{r}, k_b)$ can also be determined by the references such as uniform background k_0. The iterative methods, such as the Newton-type Distorted Born Iterative Method (DBIM) approach [87], can be used to refine an initially guessed wave number $k_b(\mathbf{r}')$ using the forward solver to predict the pressure field and inverse solver to correct the guessed wave number profile $k(\mathbf{r}')$. The termination criterion depends on the relative residual error (RRE), which is defined as:

$$\text{RRE} = \frac{\|p(\vec{\rho}, k) - p(\vec{\rho}, k_b)\|}{\|p(\vec{\rho}, k)\|}. \tag{24}$$

4.2. USCT Experiment

The experimentally validated results [70] were conducted inside a water tank with the fixed transmitting transducer and one receiver attached by a circular arm and can be rotated around the sample as the scatterer. The experimental setup is described in Fig. 3(c). Both the transmitting and receiving transducers

were unfocused plane piston radiation sources, as described in Fig. 3(a). The characteristic acoustic length $ka = 6.65$ indicates the relatively uniform field covering the object to be imaged in both transmission and reception. The signal generator sent a one-cycle sinusoidal burst signal at a center frequency of 1 MHz, and the received signal was pre-amplified by 20 dB and filtered between 300 kHz to 5 MHz using a pulser/receiver. A General Purpose Interface Bus (GPIB)-connected digital oscilloscope was used to digitize and synchronize the signals from the receiving transducer. The temperature inside the water tank was fixed at approximately $18.1°$C. The imaging target was a phantom built using a soft rubber balloon filled with a saline solution. The speed of sound of the balloon film and saline solution was determined by time-of-flight (TOF) measurements under a frequency of 1 MHz, and the speed of sound (SoS) values were measured as 1540 m/s and 1718 m/s, respectively. Additionally, the thickness of the soft rubber film and the diameter of the total balloons are 0.23 mm and 7.3 mm, respectively, with an electronic caliper. The fixed center distance between the transmitting transducer and the circular balloon was 104 mm, and the distance between the balloon phantom and the receiver was 91 mm, respectively. With this arrangement, the L-shaped arm is rotated from $-60°$ to $60°$ with a rotation step of $1°$. Two sets of measurements were collected, including the incident field without the soft balloon and another total field when the object was introduced into the water tank environment. As shown in Fig. 3(d), the scattered field was obtained by subtracting the incident field from the total field. By performing the Fourier transform along the receiving angle from the receiver positions, the amplitude and phase spectrum can be reconstructed. As shown in the center part of Fig. 3(d), imagine that we draw a line at zero angle, the first bright spot corresponds to the echo peak (Fig. 1(b)), which is much larger than the time resolution of 1 µs at a frequency of 1 MHz. In this situation, the distance uncertainties are related to the spot size, and the deep sub-microsecond time resolution is expected to be achieved by choosing the proper weight of the pulse train over a given time window. Similar to that discussed in plane wave compounding and nonlinear beamformer-based non-coherent noise reduction in the following paragraphs, the peak finding method by repetitive measuring of the diffraction field can be applied here to further improve the spatial resolution in the future. Then, the DBIM method of moment (MoM) forward solver was chosen for 0.64 MHz and 1.2 MHz phantom model reconstruction. Besides, the frequency hopping was required for the coarse reconstruction to reduce the root mean square error (RMSE). To use the operator-independent acquisition and enhanced field of view, fast volumetric ultrasound has been proposed for high-resolution 3D ultrasound tomography and reconstruction by distributed beam-formation with four 256-channel nodes with a GPU in each node [88]. The aforementioned imaging technique with separate transmitters and receivers gained widespread attention in the early stages of ultrasound imaging, particularly in breast and prostate nodule imaging. However, to make ultrasound more real-time and portable, traditional ultrasound tomography cannot meet the demands of rapid clinical diagnosis. As a result, the pulse-echo mode based on the delay-and-sum algorithm has been rapidly developed. The next part will discuss the development from pulse-echo estimation to dynamic beamforming.

5. FROM PULSE-ECHO ESTIMATION TO DYNAMIC BEAM-FORMING WITH EFFECTIVE MEDIUM

5.1. Reflection-Based B-Mode Ultrasonography

Different from USCT, reflection-based B-mode ultrasonography based on reflection and scattering has become an important adjuvant for the clinical assessment of soft tissues. Delay-and-sum (DAS) is the most widespread digital beamformer in high-frame-rate/ultrafast ultrasound imaging [2, 89, 90]. Before the widespread use of delay-and-sum algorithms in medical ultrasound transducers, beamforming was a spatial domain filtering technique primarily used in wireless communication systems to enhance signal transmission quality and efficiency. By adjusting the phase and amplitude of each antenna element in an array, a strong signal beam can be formed in a specific direction while suppressing interference and noise from other directions, which enables efficient data transmission. Beamforming is particularly important in multi-antenna systems [91] as it effectively mitigates multiple access interference and is a key technology in the physical layer of next-generation broadband wireless MIMO communication systems. The principle of the DAS beamformer is depicted in Fig. 4(a). Assuming a medium consisting of pointlike Rayleigh scatterers, the backscattered signals from these scatterers (i.e., secondary sources) are received by each array element along different travel paths. Delays can be estimated by calculating the round-trip TOF towards and from the scatterers to the transducer array elements, assuming a homogenous medium with a uniform speed of sound ($= c$). Furthermore, the two-way travel times for a scatterer of coordinates $X_s = (x_s, z_s)$ are defined by the following formula [92]:

$$\tau_i(X_s) = \frac{d_{TX}(X_s) + d_{RX}(X_s, x_i)}{c} - t_0. \tag{25}$$

d_{TX} and d_{RX} are the transmission and reception distances, respectively. In diverging wave imaging, the transmission distance d_{TX} can be expressed as the function of the virtual source as follows:

$$\begin{aligned} d_{TX}(X_s) &= \sqrt{(x_s - x_0)^2 + (z_s - z_0)^2} \\ &\quad - \sqrt{\mathrm{H}(|x_0| - L/2)(|x_0| - L/2)^2 + (z_0)^2}, \end{aligned} \tag{26}$$

where H represents the Heaviside step function that can be utilized to reduce the distance to z_0 if $|x_0| < L/2$, which indicates that the virtual source (x_0, z_0) is located behind the array transducer. The above transmission distance formula is based on a diverging wavefront. If we define a virtual source with a tilt angle of θ and a beam angle of β, the virtual source point can be rewritten as follows:

$$\begin{cases} x_0 = (L/2)\sin(2\theta)/\sin(\beta), \\ z_0 = -(L/2)\cos(\beta) + \cos(2\theta)/\sin(\beta). \end{cases} \tag{27}$$

Substituting Eq. (27) into Eq. (25), and taking the limit as $\beta \to 0^+$, the transmission distance for plane-wave imaging is

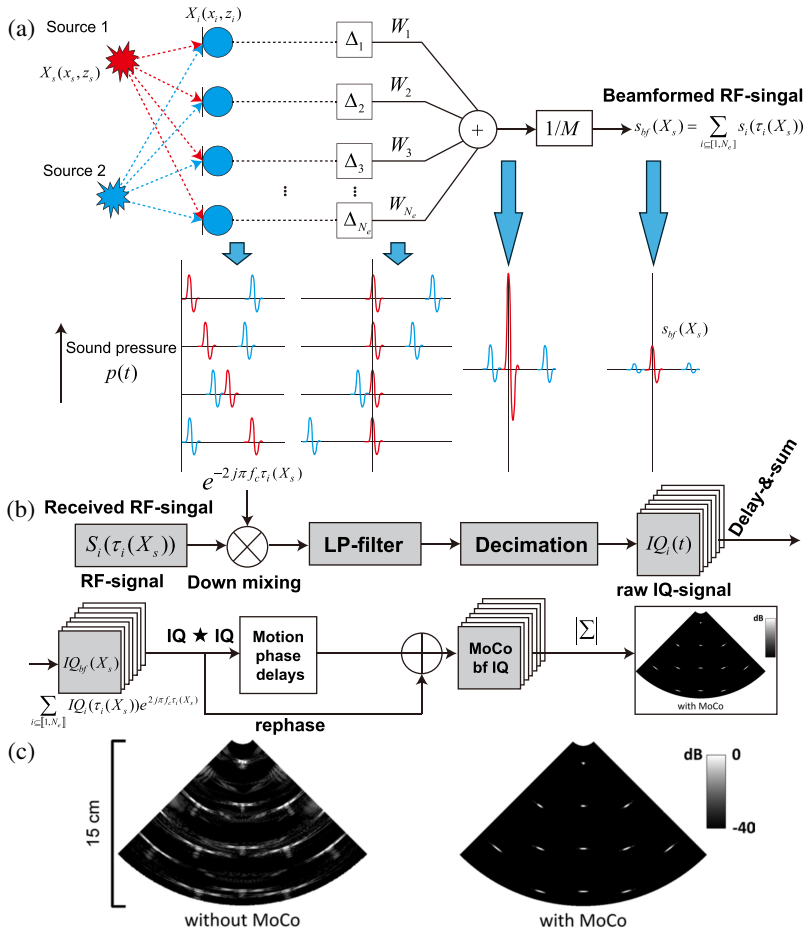

FIGURE 4. DAS beamforming and I/Q demodulation. (a) DAS beamforming from secondary sources to beamformed RF signals by DAS. (b) Raw in-phase (I) data and quadrature-phase (Q) data by I/Q demodulation have been transferred into beamformed IQ data by delay and sum (DAS). Motion phase delays are introduced to rephase the B-mode image, and the beamformed IQ refers to further motion corrected to a single image. (c) B-mode image within 15 cm shows two cases without and with motion correction (MoCo), where the motion artifacts have been removed. Panels (b) and (c) were adapted based on permission from [59].

as follows:

$$\lim_{\beta\to 0^+} d_{TX}(\mathbf{X}_s) = (\mathrm{sgn}(\theta)L/2 - x_s)\sin(\theta) + z_s\cos(\theta). \quad (28)$$

The travel distance between scatterers and receiving array elements can be given by $d_{RX}(X_s, x_i) = \sqrt{(x_i - x_s)^2 + z_s^2}$. As shown in Fig. 4(b), the analog signals received by piezoelectric elements are commonly referred to as RF (radio frequency) signals. Combining Eq. (25), the recorded signal $S_i(\tau_i(X_s))$ is pre-amplified and sampled before being processed by a beamformer. In the following algorithms, the band-pass modulated signals s_i is defined by $s_i(t) \equiv s(x_i, t)$. These signals are composed of a complex envelope of s_i which can be modulated by IQ demodulation by downmixing and low-pass filtering. The DAS-beamformed RF data at position $X_s = (x_s, z_s)$ can be written as:

$$s_{bf}(X_s) = \sum_{i\subseteq[1,N_e]} s_i(\tau_i(X_s)), \quad (29)$$

where the subscript 'bf' represents 'beamformed' and a subset of 1 to N_e considered the element directivity by using an f-number. The beamformed signals for Eq. (25) only represent the RF signals. In many situations [92, 93], the received digital RF signals will be digitally I/Q demodulated before DAS beamforming, as shown in Fig. 4(b). The received raw RF signals $[S_i(\tau_i(X_s))]$ are firstly down-mixed with the low-frequency carrier wave $[\mathrm{e}^{2\mathrm{j}\pi f_c \tau_i(X_s)}]$, followed by a low-pass filter and decimation into raw IQ signals. Taking into account the f-number, the DAS equation can be described as:

$$IQ_{bf}(X_s) = \sum_{i\subseteq[1,N_e]} IQ_i(\tau_i(X_s))\mathrm{e}^{2\mathrm{j}\pi f_c \tau_i(X_s)}, \quad (30)$$

where i is the subject to $z_s/2\,|x_s - x_i| \geq f_\#$ and $f_\# = z/\text{aperture}$. The DAS matrix is used as a linear operator that transforms the I/Q signals (IQ_i with $i = 1...N_e$) recorded by array elements (the matrix size is $n_s N_e \times N_e$) to beamformed I/Q data (IQ_{bf}). The DAS beamforming can be written as: $IQ_{bf} = M_{\mathrm{DAS}} \times IQ$, where M_{DAS} is the DAS matrix containing the interpolation weights. If a q-point interpolation is used to estimate the signals at $\tau_i(X_s)$, then the sparsity of the DAS matrix verifies:

$$\mathrm{sparsity}(M_{\mathrm{DAS}}) \geq 1 - \frac{q}{n_s}. \quad (31)$$

Sparse matrix-vector multiplication (SpMV) can be computed on GPUs [94]. Its computational complexity can also be calculated [95]. Additionally, some ultrasound tomography techniques are mathematically congruent to training a fully connected convolutional neural network with complex-valued weights and some symmetry properties. This fact means that it takes full advantage of the NVIDIA GPU technology and leads to a speed of approximately 60 to 100X over published algorithms while using 64 times fewer compute nodes (two NVIDIA GPU cards instead of 128 compute nodes). Due to the planar wave ultrasound transmission mode, the use of synthetic focusing is significantly affected by the motion of the scatterers, which interferes with the image quality of coherent compounding imaging. Particularly, motion speeds of up to 20 cm/s can be observed in the myocardial imaging process. To correct the phase delays caused by such motion, a motion-compounded (MoCo) imaging algorithm is proposed as shown in Fig. 4(b). In order to visualize the real-time tracking process of moving targets, it is first necessary to determine the autocorrelation function of the phase delays caused along the emission compounding number M. In this study, the transmit-to-transmit phase delay caused by motion can be calculated using the product of the following phase angles:

$$\phi_{\text{MoCo}}(\theta, r) = \frac{1}{2}\angle\{\mathfrak{M}_1\mathfrak{M}_2\}, \tag{32}$$

The factor $\frac{1}{2}$ is necessary to recover the phase due to the product of the two autocorrelations. The following equation shows the sum of the M migrated complex envelopes $\widetilde{s}_m(\theta, r)$ to obtain the coherently compound complex envelope:

$$\tilde{s}_{\mathcal{C}}(\theta, r) = \sum_{m=1}^{M} \left\{ \widetilde{s}_m \left(\theta, r + \left(m - \frac{M}{2} \right) \frac{\phi_{\text{MoCo}}}{4\pi} \frac{c}{f_0} \right) \mathrm{e}^{\mathrm{i}m\phi_{\text{MoCo}}} \right\}. \tag{33}$$

The effectiveness of motion correction is demonstrated in Fig. 4(c), where motion artifacts are significantly reduced, leading to clearer B-mode images. With the demand for high-resolution imaging of intracranial microvessels by using power Doppler, Kou et al. [96] proposed null subtraction imaging (NSI) based on a nonlinear beamforming technique, as an alternative to delay-and-sum (DAS). The spatial resolution has been improved by approximately six times, while the computational cost has merely increased by 40% compared with power Doppler.

5.2. Assumption and Challenges in DAS

Note that we assumed a constant speed of sound in the aforementioned DAS beamformer. The DAS beamformer assumes that the travel path between the pulse and receiver system is one line, without diffraction, aberration, and scattering. However, uncertainty exists in the transmission path through scattering media, which is primarily caused by off-axis wavefronts introduced by focused beams and the inherent anisotropy, attenuation, and absorption of the medium [97]. Additionally, higher-order phase aberrations caused by nonlinear propagation in a heterogeneous attenuating medium can contribute to signal misalignment and cause degradation of the ultrasound images [98]. In addition, in deep tissue photoacoustic computed tomography (PACT) imaging, DAS is also a widely used beamformer, although time reversal (TR) provides a more complete reconstruction, but with a greater computational cost [99]. Therefore, it is crucial to establish a sound speed model to understand the wave propagation path for accurately reconstructing ultrasound images. The accuracy of estimating the speed of sound in scattering media largely depends on the signal-to-noise ratio arising from the round-trip time between the transducer and the backscattering medium and the echo intensity. In general, the speed of sound in human tissues can be categorized into the following types: fat tissue (1435 m/s), muscle tissue (1595 m/s), blood vessels (1616 m/s), blood (1580 m/s), bones (2500 m/s), and the liver (1567 m/s) [100]. Methods for estimating the speed of sound in human tissues can be broadly divided into two categories: pulse-echo estimation based on reflection [101, 102] and insertion replacement based on through-transmission system [103–105]. The advantage of using the pulse-echo mode to evaluate the speed of sound is that it is difficult to accurately measure the mean speed of sound or the axial variations in a layered medium. Transmission-mode ultrasound tomography allows precise measurement of axial and lateral variations in the layered medium; however, this technique is limited by the transmission of ultrasonic waves and cannot be easily integrated into a system. Recently, coherent-based average sound speed estimation methods in two-layered [106] and multi-layered media [100] have been proposed for providing quantitative mapping of ultrasound images. In quantitative ultrasound imaging, the speed of sound and density can contribute to the effective acoustic impedance values that can be utilized for ultrasound estimation and imaging. Recently, some 3D-printed tissue-mimicking materials have been fabricated and measured based on ultrasound transmission-mode and pulse-echo mode characterizations at frequencies within 3.5 MHz as follows [107]: Agilus30 (2035 m/s), Formlabs (2591 m/s), VeroClear (2473 m/s), etc. The two-phase medium is based on the effective medium theory (EMT), which was initially developed by Kuster and Tokoz in the field of geophysics [108]. In this study, the velocity and attenuation of seismic waves in two-phase media have been proposed based on the density ρ_{ag} and compressibility κ_{ag} of the new effective particle based on EMT. Similar to geophysics, red blood cells contained in plasma can also be described via two fluids with acoustical properties: ρ_1, ρ_2, κ_1, and κ_2, respectively. The internal concentrations of red blood cells within the aggregates ϕ_i are as follows: $\rho_{ag} = \phi_i\rho_1 + (1-\phi_i)\rho_2$ and $1/\kappa_{ag} = \phi_i/\kappa_1 + (1-\phi_i)/\kappa_2$. In this case, the derived equation from geophysics corresponds to the effective modulus and static effective densities proposed in Section 2. Here, the nonuniform and non-Hermitian nature of material properties have not been considered, which will be discussed in the next part on ultrasound propagation in aberration layers. In this case, speckle elimination can be achieved by enhancing the non-coherence of the field, while resolution enhancement can be achieved by enhancing the spatiotemporal coherence through time-reversed focusing.

6. CHALLENGES IN ULTRASOUND PROPAGATION THROUGH ABERRATION LAYERS

6.1. Van Cittert-Zernike Theorem in Random Scattering Media

The Van Cittert-Zernike theorem is a formula in statistical optics that can predict the autocorrelation function of the wave field generated from a scattering medium illuminated by any acoustical (or optical) source [111]. The Van Cittert-Zernike theorem is one of the most important theorems of modern optics. This theorem pointed out that the wavefront from an incoherent source will appear almost coherent at large distances, but with complicated interactions near the center of the sources. The covariance of the optical field based on spatial coherence is related to the well-known Young's slit experiment and is fully described in [112]. Considering two points at X_1 and X_2 on the plane of the holes, the physical phenomenon is that the spatial covariance of the field is infinitely narrow at the incoherence source and becomes wider and wider at the far field. The Van Cittert-Zernike theorem describes that the spatial covariance of the optical field at points X_1 and X_2 is equal to the Fourier transform of the source aperture function, with a spatial frequency of $(X_2 - X_1)/\lambda Z$. In medical ultrasound, for diffuse targets, by applying the Van Cittert-Zernike theorem, the ultrasound backscatter intensity distribution is equal to the squared amplitude of the product of the ultrasound beam pattern and the target function given by the formula below [113]:

$$R(\Delta\mathbf{X}_a, z, f) = \iint_{-\infty}^{+\infty} |P(\mathbf{X}_s, z, f)\chi(\mathbf{X}_s, z, f)|^2 \times \mathrm{e}^{-2\pi \mathrm{j}(\mathbf{X}'_s \Delta\mathbf{X}_a)/\lambda z} \mathrm{d}\mathbf{X}_s, \quad (34)$$

where $\Delta\mathbf{X}_a = [x_a, y_a]^T$ represents the distance between two points X_1 and X_2 at the aperture plane of the transducer array. The diffraction field coordinates can be written as $\mathbf{X}_s = [x_s, y_s]^T$, and $\chi(\mathbf{X}_s, z, f))$ is the object function.

6.2. Time Reversal Mirror and Distortion Matrix

Mallart and Fink generalized the Van Cittert-Zernike theorem in pulse-echo measurements for ultrasound imaging [114]. In this case, the speckle noise that limits the ultrasound imaging and tissue characterization can be attributed to random interferences (stochastic nature of media) and is linked to the spatial coherence of ultrasound beams. This problem of speckle reduction can be solved using incoherent processing techniques. By applying the Van Cittert-Zernike theorem, the SNR can be defined as:

$$\mathrm{SNR} = A_R A_T \Big/ \left(\int [R_P(\mathbf{x})]^2 R_{O_R}(\mathbf{x}) \mathrm{d}\mathbf{x} \right)^{1/2}, \quad (35)$$

where A_R and R_T are the areas of the receiver and transmitter, and R_{O_R} is the receiver autocorrelation function. $R_P(\mathbf{x})$ is the spatial covariance, which is a separable function of $x_1 - x_2$ and of frequency. The detection of random scattering media (speckle noise) meets significant challenges including microcalcifications. One promising technology based on the iterative time reversal technique can be applied to compensate for the sound velocity heterogeneity and wave distortions. In this case, the random medium scattering field can be described by using the spatial covariance of the scattering field. In random scattering media with aberration layers, acoustical time-reversal invariance of the wave field can be used for precise control, guiding sound waves to propagate through randomly inhomogeneous media or reverberation tubes containing a large number of scatterers. During the process of time-reversal acoustics, sound waves undergo initial emission from the transmitter array, while the receiver array records the time-reversed wavefront information. The wave was then re-emitted and focused on the random medium, repeating multiple times to achieve maximum time compression and spatial focusing. Compared with other backpropagation algorithms, the advantage of time reversal lies in not needing prior information about the medium. By simply comparing the correlation of the transmitted and received signals before and after, the phase information of the transmitted wavefront can be modified to adapt to the spatial inhomogeneity of the aberration layers. The early ultrasound time-reversal theory was proposed by Mathias Fink and others [115]. Later, Derode et al. [116] introduced the first time-reversal acoustics experiment under high-order multiple scattering. By placing 2000 steel rods in water, they firstly demonstrated the reversibility of the high-order multiple scattering of transient sound waves. The observation resolution of the waveforms recovered through time reversal was approximately 1.05 mm, which is one-sixth of the resolution based on the classical Sinc function aperture resolution, i.e., $1.2\lambda z/a = 6.38$ mm. In the distortion matrix correction algorithm [109] used in three-dimensional ultrasound matrix imaging (UMI), the projection focusing matrix $\mathbf{R}$ between the input and output is used as a reference basis. Subsequently, the wavefront distortion caused by the focusing matrix $\mathbf{R}$ is extracted and compared with the speed of sound in an ideal homogeneous medium, ultimately resulting in the distortion matrix $\mathbf{D} = [\mathbf{D}(\mathbf{u}, \mathbf{r})]$. The distortion matrix $\mathbf{D}$ contains the aberrations caused when the wavefront is focused at any point, and is represented relative to the reference basis. The long-range correlation exhibited by this distortion matrix is similar to isoplanicity in optics. In approximate scenarios, such as a single layer of porcine tissue, the input and output point spread functions are assumed to possess spatial invariance. The iterative phase inversion algorithm provides a process for estimating the transfer matrix $\mathbf{T}(u)$, considering the differences between the input focusing point and the midpoint. By applying this algorithm to two-dimensional ultrasound matrix imaging, the original image and the reference image under 2D UMI for the same target located at 38 mm from the ultrasound sources are displayed on the right side of Fig. 5(a). To demonstrate the ability of aberration layer correlation imaging in three-dimensional UMI, a phantom composed of nylon rods and an anechoic structure was covered by a layer of porcine tissue consisting of fat and muscle tissue, serving as the aberration layer, as shown in Fig. 5(b). Additionally, a more general approach involves using a plexiglass layer on top of a human tissue-mimicking phantom to contact the transducer surface to directly collect the reflection matrix $\mathbf{R}$, which is constructed by forming a plane wave beam applied by the

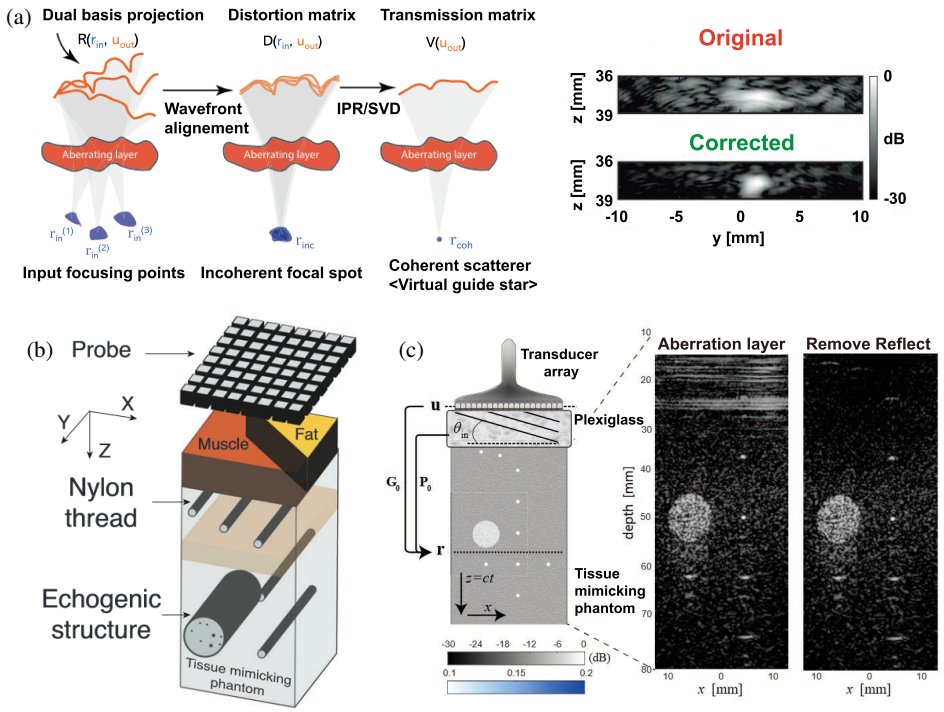

FIGURE 5. Ultrasound matrix imaging (UMI) through aberration layers. (a) UMI consists in a projection of the focused R-matrix in a correction (here transducer) basis at the output. The resulting dual R-matrix connects each focusing point to its reflected wave-front, and subsequently consists in realigning those wave-fronts to isolate their distorted component from their geometrical counterpart, thereby forming the D-matrix. An iterative phase reversal algorithm provides an estimator of the T-matrix between the correction basis and the midpoint of the input focusing points considered in the panel. The right panel exhibits the original and corrected images of the same target with 2D UMI, respectively. (b) Schematic of a tissue-mimicking phantom through pork tissue. (c) Sketch of the experimental acquisition. An ultrasonic transducer array is placed in contact with a plexiglass layer, which is on top of a human tissue-mimicking phantom. Original ultrasound confocal image and the removal of multiple reflections are shown with $c = 1800$ m/s. (a), (b) were adapted based on permission from [109]. (c) was adapted based on permission from [110].

transducer. The reflection matrix constructed in this manner can be represented as $\mathbf{R}_{kk}(z) = \mathbf{T}(z) \times \Gamma(z) \times \mathbf{T}^{\top}(z)$, where $\Gamma(z) = [\Gamma(x, x', z)]$ represents the scattering matrix inside of the phantom medium and $\mathbf{T}(z)$ is the true transmission matrix between the Fourier basis and the focal plane at the depth of z. In the coordinate illustration as shown in Fig. 5(c), it is noted that reverberation signals appear due to multiple reflections between the bones and human tissue. Interestingly, the norm-square of its coefficients directly yields the spatial frequency spectrum of the scattering medium at depth of z:

$$|R(k_{\text{out}}, k_{\text{in}}, z)|^2 = |\tilde{\gamma}(k_{\text{out}} + k_{\text{in}}, z)|^2 . \tag{36}$$

It can be noticed that reflection matrix $\mathbf{R}_{kk}$ is a sparse matrix that can be utilized to filter out signals from reverberation, and then the inverse operation can be applied to the filtered matrix $\mathbf{R}'_{kk}$ to obtain a filtered reflection matrix as follows:

$$\mathbf{R}'_{xx}(z) = \mathbf{T}_0^{\dagger}(z) \times \mathbf{R}'_{kk}(z) \times \mathbf{T}_0^{*}(z). \tag{37}$$

Compared with the original reflection matrix $\mathbf{R}_{xx}$, the low-spatial frequency component was removed from the diagonal direction of the original matrix. The removal of multiple reflections has enabled the discovery of previously hidden objects at shallow depths to recover the image information from aberration layers. The images recovered from the aberration layers are shown on the right part of Fig. 5(c). The distortion matrix approach is a powerful tool for imaging through a heterogeneous medium with a priori unknown characteristics. Aberration can be corrected without any prior knowledge of the bulk modulus or speed of sound distribution inside the phantom medium. This distortion matrix work was inspired by the original imaging work in optics [117]. Other works related to time-reversal mirrors have also been proposed for both ocean noise-based algorithms [118, 119] and ultrasound-disordered media based on the cocktail party problem [120].

6.3. Transcranial Ultrasound

As a representative example in aberration-correction ultrasound, transcranial ultrasound faces great challenges by using simple linear transducer arrays without phase modulation. Since the first introduction of time-reversal acoustics applied in human skull focusing [115, 121], researchers found one possible pathway for manipulating ultrasonic waves through aberration layers (Fig. 6(a)). A noninvasive method for focusing ultrasound through the human skull was proposed by Clement and Hynynen [122] using CT scans of the head. Recently, the transcranial focused ultrasound has also attracted attention in ultrasound stimulation by using low-intensity transcranial focused ultrasound (tFUS) as a new non-invasive brain stimulation method [123] together with low-intensity pulsed ultrasound (LIPUS) [124], which can also be applied, espe-

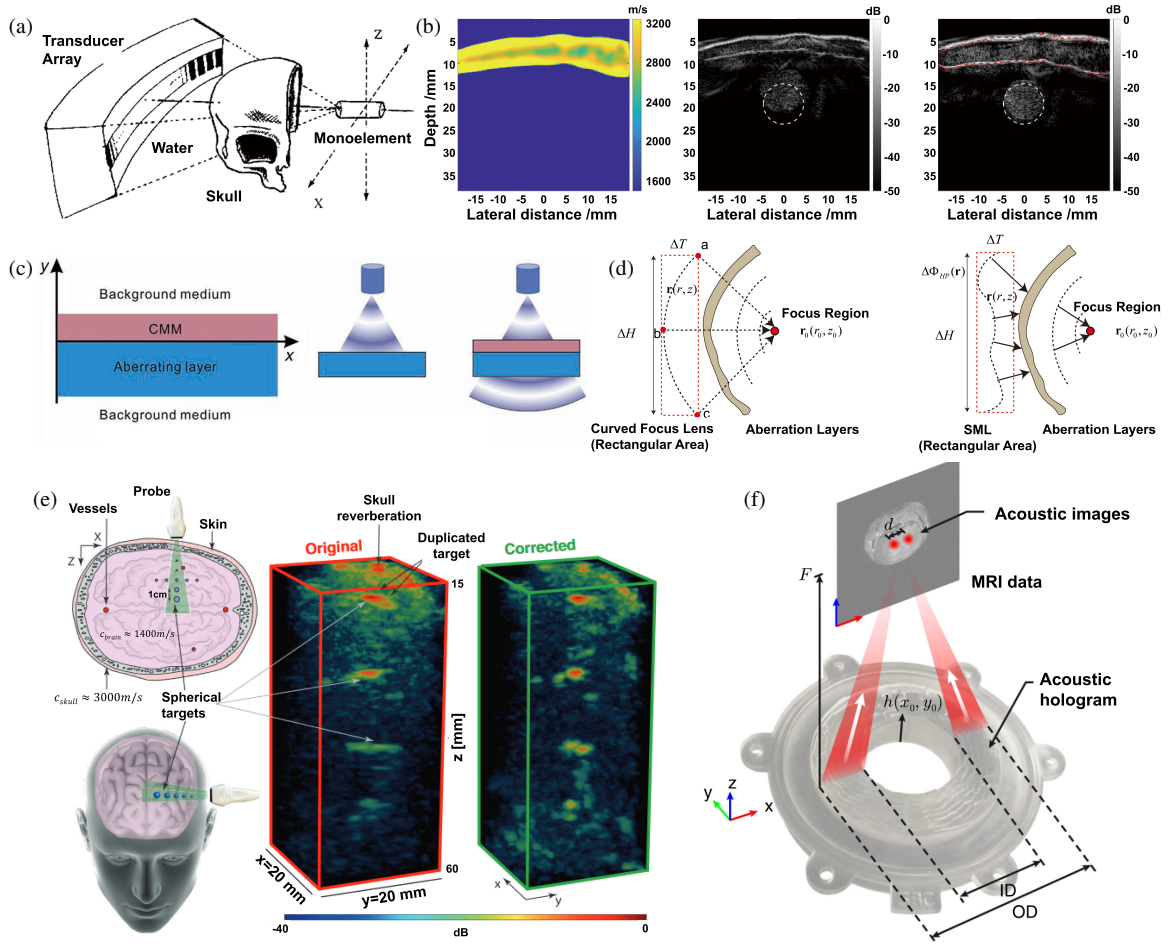

FIGURE 6. Transcranial ultrasound focusing techniques. (a) Schematic of time-reversal mirrors utilizing multi-element transducer arrays for skull focusing. (b) Simulation of sound speed distribution in the skull region, comparing images with and without aberration correction. (c) Complementary metamaterials design for wave transmission through planar aberration layers. (d) Holographic metalens design using the time-reversal method for arbitrary aberration layers. (e) Experimental configuration for transcranial imaging: top and oblique views of the setup, along with original and ultrasound matrix images through a human skull phantom. (f) Photograph of a 3D-printed holographic plate (using translucent resin) with its thickness profile defined by the function $h(x_0, y_0)$. Adapted from [42, 43, 109, 132, 133], and [134].

cially in sonogenetics [125]. In addition, based on the concept of acoustic lenses, silicone has been used to fabricate adaptive acoustic lenses for transcranial ultrasound therapy based on computed tomography by single-element transducers [126]. Since MRI and CT are widely used to provide complementary tools for imaging and reconstruction of the human brain with high spatial resolution, full-waveform inversion (FWI) imaging has also been proposed for the human brain [127] and breast [128]. In this work, 3D tomography array transducers attached to the surface of the human skull are used for data collection and transient pulse reception. FWI is an imaging method that was first widely applied in geophysics [129], and then applied to transcranial ultrasound. The computational effort required for 3D FWI was considerable. The results of using FWI for computing acoustic wave speed mapping require around 32 hours of elapsed time to complete, running on a conventional cluster of 128, CPU-based, and 24-core compute nodes. Therefore, the individual high-performance GPU-based servers are currently able to achieve speeds in excess of one peta-flop, so that they can produce a final model which is less than 10 minutes. For the full-wave simulation model, there is still a lack of a complete model to calculate the imaging capability of three-dimensional cranial bones. On the other hand, this is due to the lack of acoustic attenuation models and also the limitations in computational power based on CPUs. Based on the quantitative assessment of the human liver and skull bone, Muller et al. proposed quantitative viscoelasticity mapping by using supersonic shear wave imaging [130] and nonlinear resonant ultrasound spectroscopy (NRUS) [131], respectively. Apart from the aberration correction algorithms, recent work on ultrafast ultrasound Doppler imaging has been explored by segmenting the outer surface with a deep learning model [132]. In Fig. 6(b), firstly, the plane-wave imaging is conducted by the total region, and there is no distortion in the area above the outer surface of the skull. Then, the outer surface is segmented with the deep-learning model for B-mode imaging by the first step. The speed of the sound model of the imaging area will be updated again and imaged again. Thirdly, the inner region of the skull phantom is segmented by the deep-learning model, and the velocity model

is updated over the imaging area again. The results shown in Fig. 6(b) indicate that the sound speed distribution of the skull region has been fully reconstructed compared with the image without aberration correction in the center image; the right part of Fig. 6(b) shows the actual spatial position of the circular inclusion. By using the distortion matrix to correct the phase aberration in the skull phantom, as proposed in Figs. 5(a)–(b), transcranial ultrasound imaging of the human skull phantom has been shown in Fig. 6(e). In this case, the ultrasound probe is attached to the outer surface of the skin and images the spherical targets inside the skull phantom (c_{skull} was about 3000 m/s). Without distortion matrix correction, the skull reverberation will cause significant multi-scattering between the probe and the skull thickness region. The 3D matrix imaging results show the wavefront expansion and low imaging resolution compared with the ground truth. Using the 3D distortion matrix UMI, the real information in both the skull surface and the inner region of the soft phantom has been recovered successfully. Apart from the distortion matrix, recently, complementary acoustic metamaterials have been introduced for correcting the phase aberration over the skull-medium interfaces. As shown in Fig. 6(c), the complementary metamaterials (CMM) based on coordinate transformation is attached on the surface of the aberrating layer to mimic the human skull. The CMM compresses and cancels the information on the defined aberrating layers. The effective density tensor and compressibility of the CMM and the aberrating layers are $\rho^{(c)}(x^{(c)}, y^{(c)}, z^{(c)})$, $\rho^{(a)}(x^{(a)}, y^{(a)}, z^{(a)})$ and $\beta^{(c)}(x^{(c)}, y^{(c)}, z^{(c)})$, $\beta^{(a)}(x^{(a)}, y^{(a)}, z^{(a)})$, respectively. Based on the coordinate transformation proposed by Chen et al. [135]:

$$[\rho^{(c)}]^{-1} = \mathbf{A}[\rho^{(a)}]^{-1}\mathbf{A}^T / \det \mathbf{A}, \tag{38}$$

$$\beta^{(c)} = \beta^{(a)} / \det \mathbf{A}. \tag{39}$$

The predefined coordinate relation determines the material properties of the CMM and is expected to obtain the maximum transmission through the aberrating layers, in which the schematic diagram is shown in Fig. 6(c). The following experimental results based on the CMM have also been proposed [136]. Recently, Park et al. [137] proposed a Fabry-Perot resonance-tailoring panel to overcome the ultrasound barrier-through imaging challenges in an underwater environment. Based on the assumption of time reversal and spatial invariance, a novel spatial phase-reversal metalens design based on the virtual source setting is proposed for correcting aberrations in transcranial focusing. Compared with the traditional curved focus lens, the phase-encoded metalens can overcome the near-field correlation effect more effectively than the curved one, as shown in Fig. 6(d). Inspired by the computer-generated acoustic hologram, a very beginning research on bypassing absorbing objects in focused ultrasound by holographic techniques has been proposed by Hertzberg and Navon [138]. For a typical computer with an Intel P8700 CPU and MATLAB for 2048×2048 pixels, the calculation time was only about 2 s. Then, Melde et al. proposed one 3D-printed acoustic hologram plate for acoustic levitation and trapping objects in both air and water environments [139]. When considering the decoupled modulation of the amplitude and phase, a holey structured lossy acoustic metamaterial (LAM) has been proposed to practically implement the holographic metamaterial design [140]. Similar to medical ultrasound beamforming [141] and ultrasound-limited beam proposed by [142] in the 1990s, the broadband depth-of-field by using phase-only acoustic holograms has also been proposed for generating Bessel beams [143]. The current technology on acoustic hologram is now able to precisely target a set of focusing locations through brain disorders, such as simultaneously bilateral blood-brain barrier (BBB) opening and drug delivery in a mouse model [134]. Based on the MRI data and reconstructed acoustic model, holograms can be manufactured by stereo-lithographic 3D-printing techniques using translucent resin for BBB opening and transcranial focusing (Fig. 6(f)). The aforementioned ultrasound aberration correction algorithm aims to correct waveform distortions caused by the introduction of aberration layers. Its rapid implementation often relies on electronically scanned phased arrays or ultrafast ultrasound linear arrays. Therefore, analyzing the hardware structure of ultrasound transducers, such as an equivalent electro-acoustic network model, is more targeted for understanding the limitations of the imaging system.

7. EQUIVALENT ELECTRO-ACOUSTIC NETWORK MODEL FOR TRANSIENT ULTRASOUND WAVES AND ULTRAFAST COMPOUNDING

7.1. Ultrasound Transducer and KLM Model

In ultrasound transducer modeling, three models are widely used, including the Mason model [146, 147], the Redwood model [148], and the KLM model proposed by Krimholtz et al. [149]. The comparison between these models can be found for piezoelectric resonators in the thickness mode [150]. The KLM model uses lumped parameters to represent the equivalent electrical characteristics of piezoelectric elements and represents the mechanical properties of the structure in a transmission-line manner. By using the KLM model [144] to connect piezoelectric elements in series in the form of transmission line equations, the model can fully consider the piezoelectric crystal, backing layer, matching layer, and the connecting adhesive layer within each layer, and can independently analyze the equivalent electrical parameters of each component. In this model, the excitation voltage V_1 excites the piezoelectric crystal to generate longitudinal vibrations. After the crystal vibrates, it excites the acoustic waves. The crystal thickness in the model is d, the area is A, and the acoustic impedance of the piezoelectric crystal is z_0. When the acoustic wave encounters a scatterer and reflects back to the piezoelectric crystal, it is converted into an electrical signal using the piezoelectric effect. The equivalent electro-acoustic network model for transient ultrasound waves generated by a piezoelectric crystal has been shown in Fig. 7(a). The detailed hardware structure, including the backing and matching layers, is illustrated in Fig. 7(b). From port A, the input impedance can be written as:

$$Z_{in} = \frac{1}{\mathrm{j}wC_0} + \mathrm{j}X_1 + \frac{Z_a}{\phi^2}, \tag{40}$$

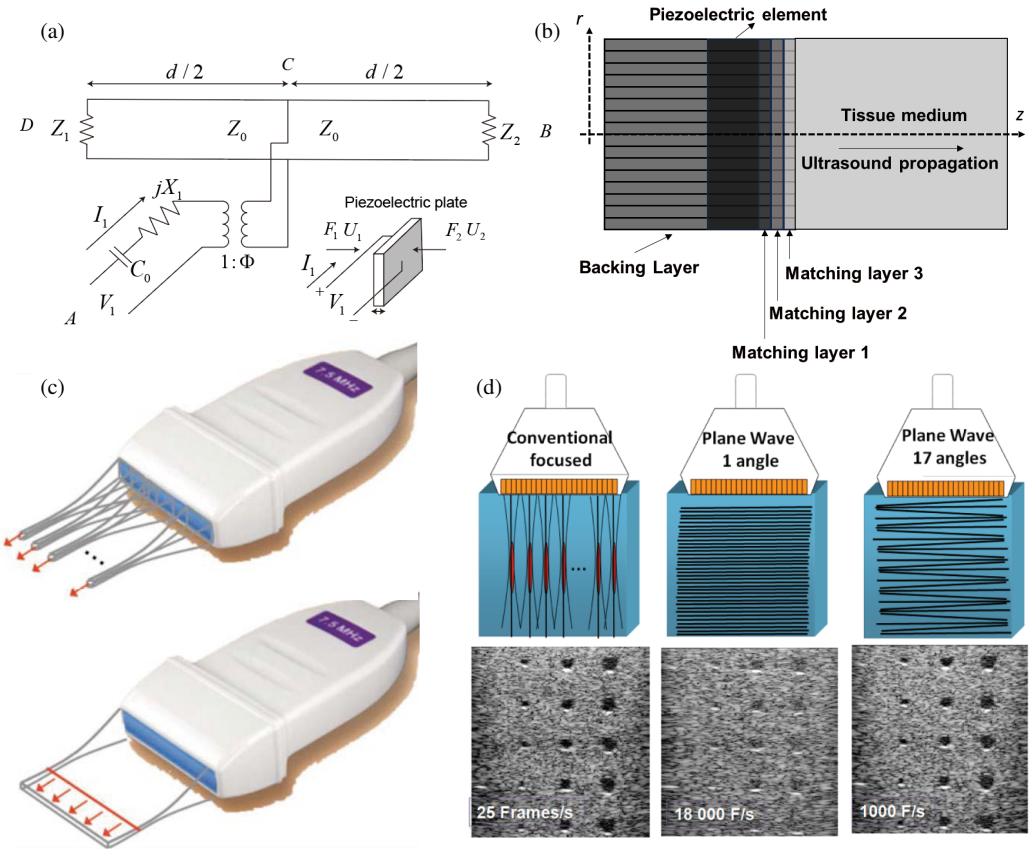

FIGURE 7. Equivalent electro-acoustic network modeling and ultrafast compounding. (a) Equivalent circuit network for simulating the impulse response of a piezoelectric plate using the KLM model. (b) Schematic diagram of the transducer hardware structure, detailing the backing layer, matching layers, piezoelectric array element, and target tissue medium. (c) Comparison of imaging modalities: conventional focused ultrasound (top) versus ultrafast plane-wave imaging (bottom). (d) Plane wave compounding using 17 angles at a 1000 fps frame rate, demonstrating improved performance over conventional focused imaging. Adapted from [144, 145], and [2].

where the capacitance C_0 and inductance X_1 can be described as:

$$C_0 = \frac{\varepsilon A}{d}, \quad X_1 = \frac{h^2}{w^2 Z_0} \sin\left(\frac{wd}{c}\right), \tag{41}$$

and the crystal impedance Z_0 and electromechanical coupling coefficient ϕ can be described as:

$$Z_0 = \rho c A, \quad \phi = \frac{wZ_0}{2h} \csc\left(\frac{wd}{2c}\right), \tag{42}$$

where ρ is the density of the piezoelectric crystal material; c is the particle velocity; ε is the permittivity constant of the material; C_0 is the capacitance; X_1 is the inductance; h is the piezoelectric constant; and ϕ is the electromechanical coupling constant. The equivalent impedance observed from point C to points D and B in the model can be written as: $Z_a = Z_{L1}Z_{L2}/(Z_{L1} + Z_{L2})$, where Z_{L1} and Z_{L2} become:

$$\begin{aligned} Z_{L1} &= \frac{Z_0(Z_1 + \mathrm{j}Z_0 \tan(wd/2c))}{Z_0 + \mathrm{j}Z_1 \tan(wd/2c)}, \\ Z_{L2} &= \frac{Z_0(Z_2 + \mathrm{j}Z_0 \tan(wd/2c))}{Z_0 + \mathrm{j}Z_2 \tan(wd/2c)}, \end{aligned} \tag{43}$$

where Z_1 and Z_2 are the acoustic impedances for the backing layer and matching layers, respectively. Taking the linear probe of a cardiac ultrasound as an example, it is mainly composed of one backing layer, one crystal layer, and three matching layers. The acoustic impedances in the crystal layer and backing layer are $Z_0 = 34.69$ MRayl and $Z_2 = 7.8$ MRayl. The acoustic impedances for the three matching layers can be chosen as 8.5 MRayl, 6 MRayl, and 3 MRayl, respectively. For the tissue medium, the acoustic impedance can usually be chosen as 1.5–2 MRayl, and the transducer area is about 448 mm^2 with 64 elements or more for the typical cardiac imaging probe.

7.2. Transient Pulse for Ultrafast Ultrasound

Similar to Positron Emission Tomography (PET), compared with computerized tomography (CT), which is a common medical scintillography technique used in nuclear medicine that uses radioactive substances known as radiotracers to visualize and measure changes in physiological activities, ultrasound wave-to-wave imaging provides a multi-mode ability for conventional ultrasound imaging [145]. The wave-to-wave imaging idea comes from the sonic shear wave and ultrasonic wave interaction that yields a highly resolved image of deep tissue stiffness. The shear wave velocity propagation in soft tissues

can be calculated by $c_s = \sqrt{\mu/\rho} = \sqrt{E/3\rho}$ and the compression wave speed can be estimated by $c_p = \sqrt{K/\rho}$. The above two formulas indicate that the shear wave speed is related to the Young's modulus of soft tissues, and the bulk modulus determines the value of the compression wave speed. In most soft tissues, the typical compression wave speed is about 1540 m/s and the shear wave speed is between 1–10 m/s. The wave-to-wave approach uses a plane wave at 500–6000 Hz pulse repetition to achieve ultrafast imaging, and the local small displacement is from 1 to 100 µm. At the surface of the phantom, there is a 50 Hz transient vibration or shear wave propagating at about 1 m/s inside the medium. Compared with the burst ultrasound excitation, the pushing force from the piezoelectric crystal to the phantom volume is approximately 6 m/s, which is faster than that of 1 m/s for shear wave propagation. When the pushing force of the transducer moves faster than the shear wave speed, the wave accumulates on a so-called Mach cone [145]. By visualizing the propagation of shear waves within soft tissue, one can infer local viscoelastic information about the tissue. However, due to the delay-and-sum algorithm-based beamformer being solely focused on the receiving end, the highest frame rate achievable with imaging modes using linear focusing (upper part of Fig. 7(c)) is approximately 30–40 fps. Delannoy et al. [151, 152] proposed utilizing parallel processing to form a complete frame image with a single acoustic pulse, achieving frame rates as high as 1000 fps. Sandrin et al. [153, 154] proposed ultrafast ultrasound imaging under planar wave illumination, with frame rates reaching up to 5000 fps (lower part of Fig. 7(c)). Conventional focused ultrasound imaging can only achieve 25 fps due to multiple focused transmissions, as shown on the left part of Fig. 7(d). In contrast, plane-wave compounding allows for ultra-fast imaging at an order of kHz. For example, using one plane-wave transmission, the imaging frame rate can reach 18 000 fps (inner part of Fig. 7(d)). However, there exists a trade-off between the image quality and frame rate. Utilizing 17 angles for plane-wave compounding (right part of Fig. 7(d)), a comparable resolution performance relative to conventional focused imaging can be achieved at a frame rate of 1000 fps. The advantage of this approach is the ability of performing high-frame-rate transient elastography imaging [155] using the shear characteristics of human tissue. Benefiting from the ultrafast frame rates ($>$ 5000 fps) for soft tissue shear wave imaging (SWI), Lee et al. proposed myocardial fiber orientation mapping using echocardiography-based SWI [156]. In addition, Lu and Greenleaf, among others [157–159] in the 1990s, proposed ultrafast ultrasound imaging using limited beams with nondiffraction characteristics, wherein the spatial Fourier transform of the object function was used to reconstruct images. In this method, speckle characteristics can be corrected using incoherent finite beams, and the spatial resolution can be improved using the principle of coherent superposition. The development of elastic wave ultrasound imaging technology is usually based on two-dimensional ultrafast ultrasound imaging. However, three-dimensional functional imaging is often limited by high computational cost and therefore low imaging speed. The complexity of an $n \times n$ matrix in a two-dimensional integral is n^2; on the other hand, the fast Fourier transform (FFT) can achieve high imaging quality with reduced computational load by sparsifying the matrix to the complexity of $n\log(n)$. FFT-based ultrasound computer holography technology and compressed sensing will be described in the next section.

In ultrasound imaging, all algorithm implementations are based on the KLM model, which is a constraint on the transducer's emission response. Under this constraint, ultrasound imaging systems can achieve B-mode imaging and elastography algorithms based on DAS. However, hardware based on the KLM model is limited to DAS and wave-to-wave, both of which have physical limitations. The introduction of acoustic holography holds promise for generating new hardware and algorithms because fundamentally, acoustic holography is not bound by the KLM-based transducer model's constraints.

8. ULTRASOUND COMPUTER HOLOGRAPHIC IMAGING AND COMPRESSED SENSING

8.1. Bessel Beams

Before the holography technology in ultrasound, it is necessary to discuss a precise solution to the Helmholtz equation, the Bessel function. Ideal Bessel beams do not undergo the diffraction process. These beams possess self-healing properties, approach the diffraction limit, and exhibit a long depth of focus. Bessel beams were first proposed by Durnin [160, 161] in 1987, and have been widely used in optics and acoustics. Moreover, the phase dislocation characteristics of higher-order Bessel beams have attracted attention in controlling the particle rotation and transmitting orbital angular momentum information. Beyond the zeroth-order Bessel function, a high-order Bessel beam with phase dislocations can be described by a pressure distribution [143]:

$$p_0(r,\theta) = \frac{1}{\sqrt{\max(r, r_0)}} \mathrm{e}^{\mathrm{i}k_r r} \mathrm{e}^{\mathrm{i}M\theta}, \tag{44}$$

where the topological charge of a first-order Bessel beam corresponds to $M = 1$, and θ is the polar angle. From the above high-order Bessel beam generation, the phase-only hologram has been mentioned for realization. From the long-range correlation property, the Bessel beam shows potential for deep-depth speckle reduction in ultrasound imaging. By applying the phase-only hologram compared with the 3D-printed Fraxicon lens, a zero-order Bessel beam with flat-intensity along the axis in the ultrasound diffraction region has been both achieved (Fig. 8(a)). However, the forward design of a Bessel beam without iterations faces great challenges in generating high-precision images when considering the interaction between the illumination pressure field and object scattering. Moreover, it also remains challenging for object reconstruction in a diffraction field is challenging.

8.2. Optical Holography

Holography, as originally conceived in optics, provides a complete framework for recording and reconstructing both the amplitude and phase of a wavefield. For acoustic applications,

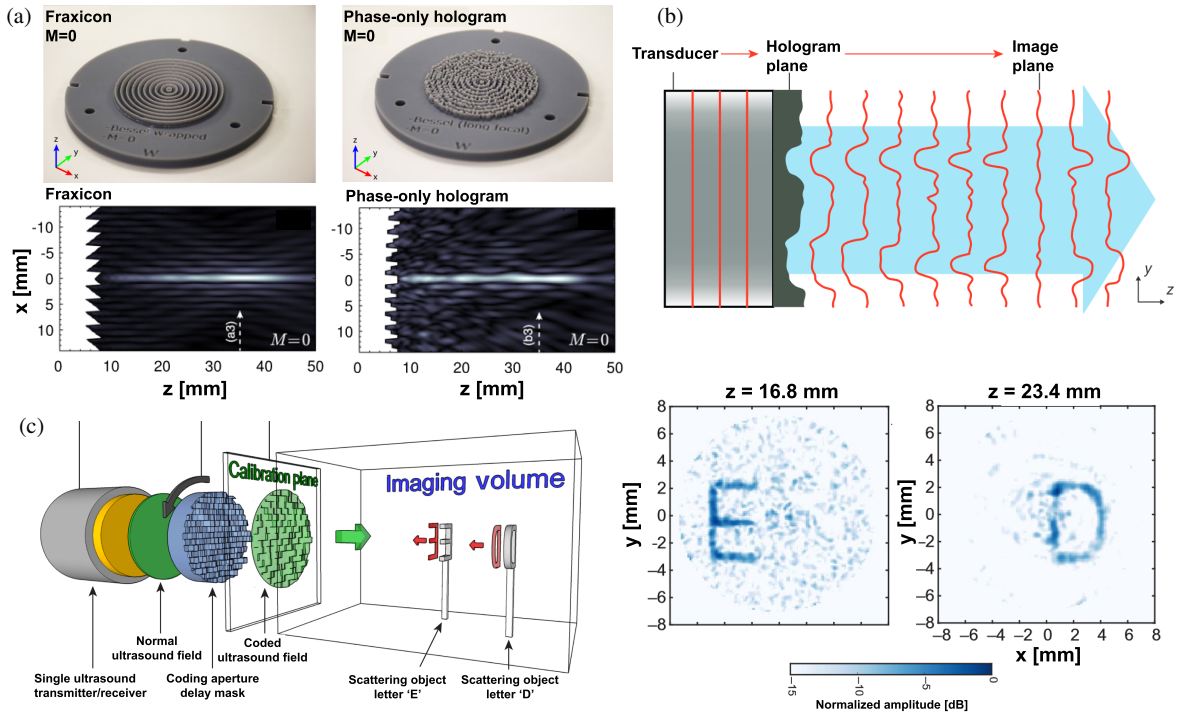

FIGURE 8. Ultrasound hologram and compressed sensing. (a) Manufactured fraxicon lens for a zero-order Bessel beam ($M = 0$) and phase-only holographic lenses for flat-intensity Bessel beams corresponding to $M = 0$. The results indicate the field distribution in the sagittal plane for the fraxicon lens and phase-only hologram, respectively. (b) Schematic diagram of a hologram plate attached to the surface of the transducer, converting a planar wavefront from the transducer into the required phase distribution. This travelling wave diffracts to form an image in the image plane. (c) Schematic overview of the complete imaging setup. A single sensor transmits a phase uniform ultrasound wave through a coding mask that enables the object information (two plastic letters "E" and "D") to be compressed to a single measurement. Rotation of the mask enables additional measurements of the same object. Result of solving part of the image vector through an iterative least squares technique. The two images are mean projections of six pixels along the z dimension (individual z slices). (a) was adapted based on permission from [143]. (b) was adapted based on permission from [139]. (c) was adapted based on permission from [44].

this capability is especially valuable because conventional ultrasound transducers typically capture only intensity (or envelope) information, discarding the phase that carries critical information about tissue structure and composition. By understanding how optical holography records the interference between a reference wave and an object-scattered wave, one can directly map this concept to acoustic holography, where a reference acoustic wave is used to encode phase information into measurable intensity patterns. This optical foundation is therefore essential for appreciating the principles behind ultrasound holographic imaging, which we discuss in the following subsection. Historically, the development of acoustic holography has closely followed advances in optical holography, making a thorough review of the optical counterpart indispensable.

To solve the above-mentioned problem, optical holography is the fundamental theory behind achieving the three-dimensional reconstruction of objects, high-density data storage, and optical manipulation of cells using optical tweezers. Essentially, holographic technology can control the coherence range and intensity distribution of the wavefront in space. Information is recorded directly or using spatial illumination, which involves holographic recording and forward propagation, respectively. Unlike TIE and ptychography, inline holography is a quantitative optical phase imaging method based on interferometric optics, which was first invented and proposed by British scientist Gabor [162] in 1948 based on the theory of wavefront reconstruction. This method involves the interference between the reference light and diffracted light from objects to record holograms on materials, which are then reconstructed and magnified by illuminating the hologram with visible light. However, due to the poor coherence of the mercury lamp used at that time and the adoption of an inline holographic system, the imaging effect was not extremely good. By the year 1960, with the introduction of laser light sources, high-coherence light sources became available, making it easier to record optical wave information. In 1964, Leith and Upatnieks proposed off-axis holography [163], utilizing the off-axis reference beam method, where two interfering light beams are at non-coaxial angles to obtain holograms, solving the problem of overlapping images from different diffraction orders in inline holography. Subsequently, scientists began diverse explorations in holography, leading to techniques such as reflection holography, color holography, and image holography [112, 164, 165], enriching holographic images with vibrant colors, and expanding the application space of holography. Due to the high coherence of laser light sources, which demands higher stability in optical systems, white-light holography has become a research hotspot, with white-light recording and reconstruction being extensively studied. Cur-

rently, holographic technology has yielded a wide range of applications, including holographic displays, holographic storage, optical tweezers, and holographic imaging. With the advancement of computers and optoelectronic devices, computational holography and digital holography have emerged. In 1967, an American scientist Goodman [166] introduced digital holography, using electronic devices instead of traditional holographic plates for hologram recording, and reproducing holographic images on computers. In 1966, German scientists Lohmann and Paris [167] laid the theoretical foundation for computational holography and produced the first computational hologram. Given the rapid development of radar communication systems, Wiley at Goodyear Aircraft company laid the foundation for the invention of a synthetic radar system for remote sensing, with the early demonstration taking place at the University of Illinois in the 1950s, a historical milestone that was retrospectively summarized in later literature [168].

8.3. Ultrasound Holography

Building upon the principles of optical holography reviewed in Section 8.2, ultrasound holography seeks to achieve analogous wavefront recording and reconstruction using acoustic waves. The key insight from optics is that by interfering the scattered field with a known reference field, one can encode both amplitude and phase information into a measurable intensity pattern (the hologram). In the acoustic domain, this same principle applies: a piezoelectric transducer array or a holographic mask can be used to record the interference pattern, and the object's acoustic properties can be subsequently reconstructed via numerical backpropagation. Thus, the optical holography framework provides not only the conceptual foundation but also the mathematical tools — such as the angular spectrum method and iterative phase retrieval — that are directly transferable to ultrasound. In this subsection, we discuss how these optical concepts have been adapted to realize acoustic holographic imaging, with applications ranging from particle manipulation to transcranial focusing.

In the early stages of optical holography, the interaction between spatially coherent beams and object scattering is recorded using photodetectors, which are primarily divided into on-axis and off-axis holography. In ultrasound holography, acquiring scattering information can be based on the product integral of the beam intensity and scattering distribution function according to the Van Cittert-Zernike theorem in multi-variable imaging, followed by holographic projection through the product of transfer functions [113]. For the one-way propagation process based on the two-dimensional aperture amplitude, the diffraction field can be written as:

$$p(\mathbf{X}_s, z, f) = \frac{\mathrm{e}^{\mathrm{j}kz}\mathrm{e}^{\mathrm{j}k(\mathbf{X}_s'\mathbf{X}_s)/2z}}{\mathrm{j}\lambda z} \times \iint_{-\infty}^{\infty} \left\{ A(\mathbf{X}_a, f)\mathrm{e}^{\mathrm{j}k\mathbf{X}_a'\mathbf{X}_a/2z} \right\} \mathrm{e}^{-2\pi\mathrm{j}\mathbf{X}_s'\mathbf{X}_a/\lambda z}\mathrm{d}\mathbf{X}_a, \quad (45)$$

where $p(\mathbf{X}_s, z, f)$ refers to the diffraction pressure patterns for the original amplitude $A(\mathbf{X}_a, f)$ at the hologram plane. One widely used algorithm is the iterative angular spectrum algorithm (IASA), considering the transducer as a multi-element array system. Holographic projection can be achieved by encoding the aperture in terms of both the amplitude and phase. Firstly, the transmission of planar ultrasound waves is represented by the following pressure-wave equation:

$$p(x, y, z) = \hat{p}(x, y, z)\mathrm{e}^{\mathrm{j}\Delta\phi(x,y,z)}, \quad (46)$$

where the initial amplitude and phase function at the imaging plane in the diffraction field are recorded as $\hat{p}$ and $\phi(x, y, z)$, respectively. Subsequently, the angular spectrum can then be obtained by the spatial Fourier transform at the imaging plane as follows:

$$P(k_x, k_y, z) = \iint_{-\infty}^{+\infty} p(x, y, z)\mathrm{e}^{-\mathrm{j}(k_x x + k_y y)}\mathrm{d}x\mathrm{d}y, \quad (47)$$

the backpropagation from the image to transducer arrays can be calculated as:

$$P(k_x, k_y, 0) = P(k_x, k_y, z)H(k_x, k_y, -z), \quad (48)$$

where the propagator function can be expressed as $H(k_x, k_y, z) = \mathrm{e}^{\mathrm{j}z\sqrt{k^2 - k_x^2 - k_y^2}}$. Here, the wave vector $\mathbf{k} = (k_x, k_y, k_z)$ represents the three wavenumber components over forward and backward propagation. Then, the forward propagation will be $P(k_x, k_y, z) = P(k_x, k_y, 0)H(k_x, k_y, z)$ and the real-space pressure field Fig. 8(b) can be obtained by inverse Fourier transform as follows:

$$p(x, y, z) = \frac{1}{4\pi^2}\iint_{-\infty}^{+\infty} P(k_x, k_y, z)\mathrm{d}k_x\mathrm{d}k_y. \quad (49)$$

The following step is to compare the image quality of the projected image and forward-propagated images. The root mean square error (RMSE) or structural similarity index (SSIM) can be used to determine whether the quality of the iterative image meets our expectations. Finally, repeat Eq. (46) and backpropagate the phase and amplitude of the ultrasonic field again until the RMSE or SSIM is below the set threshold. By applying the following algorithm, researchers can fabricate the expected metamaterial-based ultrasound transducer (Figs. 1(a)–(b)), which is becoming a hot topic in the metatransducer field [169].

8.4. Compressed Sensing and Fischer Information

Most ultrasound transducer arrays are primarily two-dimensional linear or curved linear arrays. However, to achieve three-dimensional volume imaging, it often requires rotation or translation of the 2D array. The main limitation is the high hardware complexity required for 3D ultrasound imaging, such as needing over 1024 ultrasound transducer arrays and highly integrated electronic circuits. Moreover, computational ultrasound imaging in awake mice faces great challenges in that the overall size of the acoustic matrix was computed to be approximately 40 TB and 7.7 hours reconstruction [170]. The complexity of the data acquisition depends on the sampling constraints imposed by the Nyquist

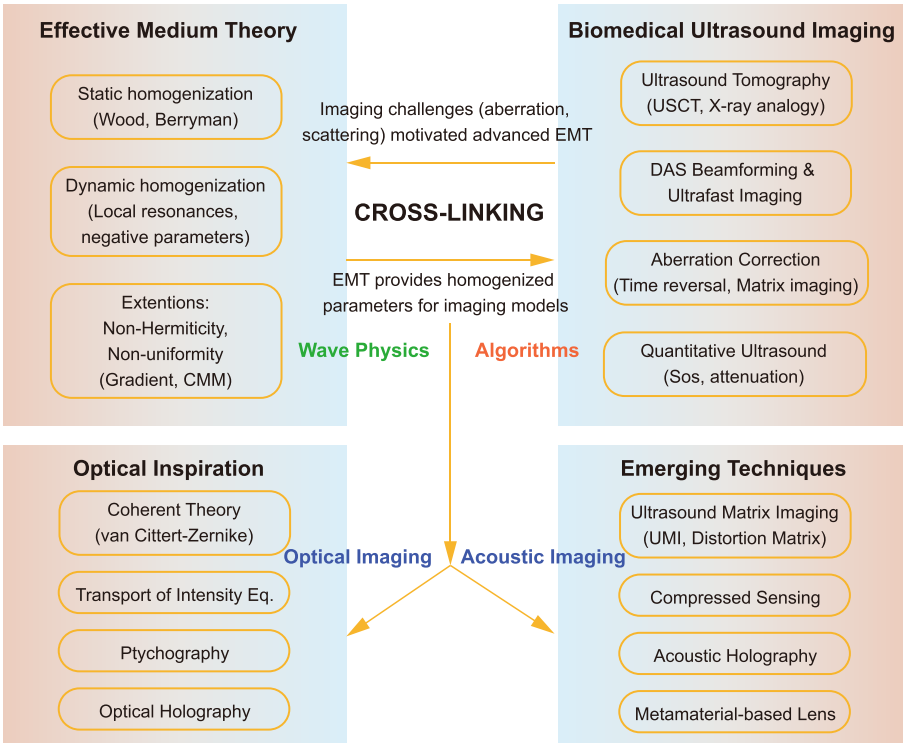

FIGURE 9. Systematic framework of acoustic computation: interconnections between effective medium theory, biomedical ultrasound imaging, optical inspirations, and emerging techniques.

sampling theorem. To overcome the constraints of the Nyquist theorem requiring uniform sampling of analog signals during digitization, it often necessitates sampling rates of more than twice the highest frequency component, which significantly increases the data volume. This limitation has opened up another new research area, known as compressed-sensing imaging. Through compressed sensing, the high-volume channel signals can be compressed several times, similar to the compression process of graphic files. Consequently, the original data volume can be drastically reduced and is no longer bound by the Nyquist sampling theorem. Inspired by the principles of compressed sensing imaging, a work on achieving three-dimensional volumetric ultrasound with a single element has put forward a rotation phase-coded aperture mask [44]. Information is encoded into measurements of random apertures and correlated signals, with decoding algorithms used for the recovery and imaging of the measurement results. As shown in Fig. 8(c), the signal matrix $\mathbf{u}$ from the pulse-echo measurements based on multiple hardware rotations can be represented as a linear combination of the measurement matrix $\mathbf{H}$ based on accurate hardware measurements and the true image $\mathbf{v}$ of the reconstructed position. The model can be expressed as the following formula:

$$\mathbf{u} = \mathbf{H}\mathbf{v} + \mathbf{n}, \tag{50}$$

where $\mathbf{u}$ is an M-dimensional matrix containing pulse-echo signals, with the matrix's rows expanded through multiple rotations; $\mathbf{H}$ is a prediction matrix based on accurate plane calibration used for forward transmission and self-convolution, and with the pulse signal calibration results after multiple rotations are used to increase the number of rows in the $\mathbf{H}$ matrix, with dimensions of $M \times N$ ($M < N$). The calibration field results from signal scans using small needle hydrophones and displacement platforms in a water tank. The initial plane calibration signal field results can be extended to arbitrary diffraction planes through information transfer and prediction using Melde's iterative angular spectrum algorithm (IASA) about holography [139]. In theory, the more rotations that are added, the more accurate the additional rows provided for image reconstruction. The complete imaging schematic is shown in Fig. 8(c), where a single sensor performs compressed sensing imaging through rotating a randomly encoded mask board. The role of the random phase mask is to disrupt the phase uniformity of the ultrasound to achieve compressed sensing imaging, with letters E and D placed at two different distances in the diffraction field as scattering targets. To reduce the overall data volume of the matrix, the 3D image is obtained through 50 rotations with uniform sampling intervals. To determine the spatial correlation of pulse-echo signals for deriving a single scatterer from single or multiple measurements, the Fisher information matrix is used to numerically compute the covariance matrix of the Cramer-Rao lower bound. Its assumptions include: 1. Any noise is considered zero-mean Gaussian white noise. 2. Adherence to the point-source superposition principle in the mask template. 3. The pulse response of the transducer is equivalent to a Gaussian signal: $h(t) = \exp[-\frac{t^2}{2l^2}]$ and emits a single Dirac pulse. The virtual source j is denoted as $\mathbf{s}_j$, and the set of all $\mathbf{s}_j$ is denoted as S. Under the above-mentioned assumption, the forward pressure field at position $\theta = [x, y, z]^T$ can be

written as:

$$p(t,\mathbf{0}) = \sum_{j=0}^{|S|-1} h(t-\tau(\mathbf{0},\mathbf{s}_j)), \tag{51}$$

where $c\tau(\theta,\mathbf{s}_j) = \frac{1}{c_1}[\mathbf{s}_j]_z + \frac{1}{c_0}||\mathbf{s}_j-\theta||_2$. Mask impulse response: $p(t,\mathbf{0}) = h(t)\star m(t,\mathbf{0},\mathbf{S})$ and the echo signal is equivalent to the autoconvolution of the forward pressure wave field $a(t,\mathbf{0}) = p(t,\mathbf{0}) * p(t,\mathbf{0})$ at θ. The (i,j)th entry of the Fisher information matrix is equal to:

$$I(\theta)_{i,j} = \frac{1}{\sigma^2}\frac{\partial \mathbf{a}(\theta)^T}{\partial[\theta]_i}\frac{\partial a(\theta)}{\partial[\theta]_j}. \tag{52}$$

Making the educated guess of signal propagation through scattered media is a fast-moving frontier in computational imaging, and the assumption of Poisson statistics of photons works well. Recently, the Fisher information matrix [171] has become a method for measuring the amount of information contained in a random variable about a parameter (such as the mean) in its probability distribution. Moreover, statistical methods in the Fisher information matrix for random scattering media and the application of the Cramer-Rao lower bound (CRLB) in computational ultrasound imaging will soon become a trend in the future.

9. CONCLUSIONS AND OUTLOOK

In this review, we present Fig. 9 as a systematic framework that integrates the main concepts discussed in our work, namely effective medium theory, biomedical ultrasound imaging, optical inspirations, and emerging techniques. The diagram is organized hierarchically from top to bottom. At the apex, we place the overarching theme — Acoustic Computation — which bridges two complementary pillars: Effective Medium Theory (left) and Biomedical Ultrasound Imaging (right). On the left, we summarize key topics in homogenization, including static and dynamic models, as well as extensions addressing non-Hermiticity and nonuniformity. On the right, we cover major imaging modalities and algorithms, such as ultrasound tomography, DAS beamforming, aberration correction, and quantitative ultrasound. A bidirectional arrow between the two pillars highlights the mutual reinforcement we have emphasized throughout the review: effective medium theory provides homogenized parameters that improve imaging reconstruction, while imaging challenges (e.g., aberration and scattering) drive the development of advanced homogenization models. This cross-linking is further elaborated in the central Cross-linking box, where we explicitly state these interdependencies. In the lower part of the diagram, we branch into two additional domains: Optical Inspiration and Emerging Techniques. The former acknowledges that established optical imaging theories — coherence theory, transport of intensity equation, ptychography, and optical holography — have inspired analogous acoustic methods. The latter lists recent technological advances, including ultrasound matrix imaging, compressed sensing, acoustic holography, and metamaterial-based lenses, which we consider as future directions for acoustic computation. Collectively, Fig. 9 provides a concise yet comprehensive roadmap of the field, illustrating how fundamental homogenization principles, imaging methodologies, cross-disciplinary inspirations, and cutting-edge techniques are interconnected within the scope of acoustic computation.

We have attempted to summarize the research developments from the effective medium theory to biomedical ultrasound imaging. Although these are two completely different research fields, the effective medium theory discusses the resonance [10, 11] and non-resonance [7, 8] characteristics of sound waves at different wavelengths and scatterer sizes from the constitutive properties of materials. In this section, the real and imaginary parts of the dynamic mass density and bulk modulus trigger local resonances in the transmission and reflection coefficients [3, 26, 27], while the increase in absorption time and interaction depth of ultrasound pulses with human tissue leads to a layer-by-layer decrease in reflectance during the ultrasound transmission process. The other part of this review emphasizes the wavefront modulation of the optical/acoustic field based on the interaction between the wave field and object functions, thereby developing transmission-based ultrasound tomography imaging [70] and reflection-based DAS algorithms [92]. The early emergence of periodic and lossless acoustic metamaterials directly facilitated the development of the homogenization theory based on multiple scattering media [8]. In recent years, this theory has evolved into a more complex and practical effective medium theory with non-Hermitian [36] and nonuniform [22, 24, 42, 172] characteristics that match the actual effective properties in biomedical ultrasound imaging. One of the research challenges is how to adaptively establish a proper material absorption model to accommodate different ultrasound imaging modes and for establishing a universal standard for different imaging modalities. We currently understand that the non-Hermitian and nonuniform nature of materials significantly affects imaging quality. However, the lack of understanding of material dispersion [107] in the ultrasound frequency range hinders the further development of this theory. Therefore, it is crucial to expand quantitative ultrasound into a more universally acceptable theoretical framework. From the perspective of computational optical imaging to ultrasound tomography, the understanding of ultrasound local coherence is still limited to integral forms based on the first-order Born and Rytov approximations [46]. Different from the optical transport of intensity equation (TIE) [51], the relationship between intensity change and local phase gradients in ultrasound imaging is not as mature. One possible limitation is that many ultrasound algorithms employ DAS algorithms similar to synthetic aperture radar beamforming [173], which are fundamentally based on the acoustic eikonal equation [174], thus overlooking the spatial coherence, diffraction, and multiple-scattering effects on the intensity. In standard B-mode imaging, the reconstruction process assumes that the propagation of energy travels in a straight line without bending or scattering. Historically, the algorithms that fully utilized this ray-based method have been well developed in geophysical exploration of oil and gas based on seismic waves and oceanographic applications [118, 119] from shallow water to the deep ocean. Furthermore, computed

tomography (CT) technology based on X-rays has made significant achievements in quantitative soft tissue imaging, fundamentally through the quantitative estimation of absorption coefficients in air and water media. This helps to determine the density distribution corresponding to the Hounsfield Units (HU) of different soft and hard tissues. Based on the experience of CT scans, ultrasound quantitative imaging has attracted attention in terms of attenuation coefficient mapping [175] and velocity mapping [100]. However, the incoherent nature of ultrasound waves in tissues causes speckle effects, as well as nonlinear absorption and frequency dispersion effects increasing with tissue depth, limiting the accuracy from intensity estimation to quantitative phase mapping and attenuation mapping. Moreover, enhancing the accuracy of quantitative estimations while understanding the diffraction field characteristics of imaging and tissue types has become a challenge that needs to be addressed in quantitative ultrasound imaging. Since the NVIDIA GeForce GPUs were first introduced in October 1999 [176], they have directly promoted the application of convolutional neural networks (CNN) in computer vision and image segmentation. By increasing the number of neurons, selecting appropriate filter convolution operators, and generalization schemes, it is possible to ensure the adaptability of image segmentation and the accuracy of feature extraction. Compared with other medical data, ultrasound imaging lacks a large number of specific datasets. Currently, there is no mature and efficient solution for applying artificial intelligence to ultrasound imaging. Therefore, we recommend using transfer-learning methods to overcome this challenge. For instance, complete datasets of CT images and disease data are already available for use and transfer. By creating a small new dataset of acoustic phantom images, we can retrain the existing models and emphasize the distinctions between optical and acoustic images. This approach enables us to leverage the dataset and accurately identify ultrasound images. Furthermore, some speckle reduction algorithms for volumetric ultrasound require multiple emissions to increase the incoherence of the diffraction field. However, they are still limited by data redundancy and CPU processing speed, making it difficult to achieve high-frame-rate volumetric imaging and real-time processing. The development of GPUs may provide a new path for the next-generation high-speed imaging and recognition using volumetric ultrasound. Aberration layers, as obstacles to energy transmission, are widely present in microwave engineering, electromagnetic waves, and ultrasonic transcranial transmission. Based on the reciprocity of acoustic waves, time-reversal mirrors [115, 121] have been proven to achieve reverse focusing and image reproduction in fluid systems and ultrasound, thereby enhancing the signal-to-noise ratio of ultrasound signals in strongly scattering media [109, 110]. The design of a novel ultrasound matching layer based on complementary media theory [43] effectively reduces the impedance mismatch at the interface between the aberration layer and background media, thereby maximizing the energy transmission. However, owing to the non-negligible high-frequency attenuation in ultrasound, further understanding of the non-Hermitian properties based on the transformation theory [177] of the medium and their impact on ultrasound transmission characteristics is of particular importance. Phase-conjugate metalenses [42] were reconstructed based on the concept of time-reversal focusing lenses, and the future development of this theory is expected to be experimentally realized using micro/nano acoustic metamaterials, potentially exerting a sustained impact in the field of transcranial ultrasound. Additionally, as human tissue is an anisotropic and nonuniform medium, ultrasound imaging continues to have an impact in areas such as bone assessment [132], gingival fiber imaging [178], artery plaque imaging [179], liver health elastography, and cardiovascular and cerebrovascular diseases, among others. The overall trend in probe development is towards miniaturization, low power consumption, and wireless direction, with the potential to expand into point-of-care medical ultrasound and personalized healthcare in the future. Ultrasound ultra-fast elastic wave compounding is a revolutionary technology in wave-to-wave imaging, benefiting from the characteristics of soft tissues that are difficult to compress but easy to shear [2, 180]. Currently, ultra-fast elastic wave compounding has been widely applied in nondestructive testing, health assessment of structural components, and cellular elastic properties. As the imaging depth increased, the signal-to-noise ratio also decreased. Maintaining imaging quality and accuracy in deep imaging areas such as the heart is a challenge, and nondiffracting X waves and Bessel beams [142, 157–159] are expected to address this challenge in the future. Achieving high-resolution and high-precision elastic wave imaging is another challenge, especially in complex effective media where nonlinear wave propagation and attenuation need to be overcome. The newly developed acoustic holography technology can effectively record all the information of the medium, offering a potential solution for high-resolution coherent imaging in the future. High-frame-rate and high-dimensional real-time ultrasound imaging is the future pursued by medical imaging, which is crucial for reducing the misdiagnosis rate of clinicians and improving the efficiency of diagnosis and treatment under ultrasound guidance. Similar to CT, MRI [181], and nuclear medicine, the field of ultrasound is experiencing explosive growth, with the industry continuously introducing revolutionary products in personalized medicine, point-of-care centers, and digital healthcare. The emergence of convolutional neural networks (CNNs) and transfer learning (TL) has provided a new pathway for the rapid segmentation of ultrasound images and fusion with CT images. Cardiovascular diseases benefit from large datasets of clinically driven cardiac ultrasound under artificial intelligence, enabling the rapid assessment of cardiovascular diseases by physicians. Recently, with the advancement of natural language processing, training and validation based on large-scale ultrasound text-image datasets have promoted the development of ultrasound report auto-generation technology [182], which holds promise for breakthroughs in alleviating the burden on healthcare and improving patient diagnostic accuracy in the future. However, owing to the data rate limitation of Peripheral Component Interconnect Express (PCIE) to GPU communication, IQ-based ultrasound signals can still not be easily processed in real-time 3D volumetric imaging. Due to the efficient transmission rate of Ethernet optical transceivers and the fast processing capability of GPUs, the hardware interface for optical microscopy imaging has matured, while the pro-

cessing speed of ultrasound signals based on IQ protocols is significantly slower than that of optical interfaces. Therefore, exploring how to fully utilize optical signal processing [183, 184] for ultrasound data could be a potential pathway toward real-time three-dimensional ultrasound imaging in the future.

All-optical ultrasound (OpUS) imaging [185] is one of the attempts to combine the fast transmission rate of optical communication and the deep penetration depth of ultrasound imaging. Recent studies have been performed on switching the ultrasound generation and receiving end to an optical fiber. Generally, optical-based ultrasound generation can be achieved by employing composite photothermal and thermal expansion thin film. To receive ultrasound signals, the change in pressure is converted into a relative change in optical response. For instance, reflectivity changes can be detected based on Fabry-Pérot interferometer [186, 187] and Bragg grating sensor [188]. However, traditional OpUS configuration is restricted to shallow depth endoscopy, including intravascular detection and oesophageal imaging [187, 188]. Nevertheless, with the rapidly growing photonic integrated circuit (PIC) technology, performing optical computation and interference imaging processing with PIC exhibits exceptional potential in applications and improved computational speed [189, 190] relative to traditional computing schemes. This spontaneously fits the optical ultrasound receiving sensors mentioned above, showing potential if introducing a receiving sensors array and connecting to a PIC. It can be foreseen that biomedical ultrasound imaging development is not only correlated with effective medium theory and computational algorithms, but its connection with multiphysics fields will also become a future development direction.

ACKNOWLEDGEMENT

N.X.F. acknowledges the financial support from the Innovation and Technology Fund (ITF) APAS platform (ITP/064/23AP), the HK Jockey Club Charities Trust (GSP 181), the HKU Materials Innovation Institute for Life Sciences and Energy (MILES), and the State Key Laboratory of Optical Quantum Materials at The University of Hong Kong. This work was also supported by the Healthy Longevity Catalyst Awards (HLCA/E-709/25), the NSFC/RGC Joint Research Scheme (N_HKU718/25), the RGC Strategic Topics Grant (STG3/E-704/23-N), and the Quantum Science Center of Guangdong-Hong Kong-Macau Greater Bay Area (GDZX2304003).

APPENDIX A. PTYCHOGRAPHY RECONSTRUCTION ALGORITHM

The algorithm proceeds from the guess of the specimen transmission function (object function) $O_{g,n}(\mathbf{r})$, where the subscripts g and n represent the guessed function and nth iteration of the algorithm, respectively. Then, the guessed exit wave function will be the product of the guessed object function $O_{g,n}(\mathbf{r})$ and the known illumination function $P(\mathbf{r}-\mathbf{R})$ for the current position $\mathbf{R}$ and the original position r:

$$\psi_{g,n}(\mathbf{r},\mathbf{R}) = O_{g,n}(\mathbf{r})P(\mathbf{r}-\mathbf{R}). \tag{A1}$$

Transform $\psi_{g,n}(\mathbf{r},\mathbf{R})$ from Cartesian space coordinate to diffraction Fourier space plane:

$$\Psi_{g,n}(\mathbf{k},\mathbf{R}) = \mathcal{F}[\psi_{g,n}(\mathbf{r},\mathbf{R})], \tag{A2}$$

where $\mathbf{k}$ is the wave vector in the optical system, which is the usual reciprocal-space coordinate. If we consider the phase term in the diffraction space at iteration n for position $\mathbf{R}$, the guessed wave function in Fourier space can be described as the product of the guessed amplitude diffraction space modulus $|\Psi_{g,n}(\mathbf{k},\mathbf{R})|$ and the guessed phase term $\mathrm{e}^{\mathrm{i}\theta_{g,n}(\mathbf{k},\mathbf{R})}$ as follows:

$$\Psi_{g,n}(\mathbf{k},\mathbf{R}) = |\Psi_{g,n}(\mathbf{k},\mathbf{R})|\,\mathrm{e}^{\mathrm{i}\theta_{g,n}(\mathbf{k},\mathbf{R})}. \tag{A3}$$

The next step is to correct the guessed diffraction space wave function to the known amplitude values,

$$\Psi_{c,n}(\mathbf{k},\mathbf{R}) = |\Psi(\mathbf{k},\mathbf{R})|\,\mathrm{e}^{\mathrm{i}\theta_{g,n}(\mathbf{k},\mathbf{R})}. \tag{A4}$$

Then, the inverse Fourier transform is utilized back to the Cartesian coordinate space for the exit wave function:

$$\psi_{c,n}(\mathbf{r},\mathbf{R}) = \mathcal{F}^{-1}[\Psi_{c,n}(\mathbf{k},\mathbf{R})]. \tag{A5}$$

APPENDIX B. BORN ITERATIVE INVERSION FOR INVERSE SCATTERING

The integral can be discretized into the form of an integral operator. Therefore, the scattered field can be further rewritten as:

$$\hat{\mathbf{p}}_j^{sct} = \mathbf{M}[\chi], \tag{B1}$$

where $\mathbf{M}$ is the integral operator. The aim of this reconstruction is to reconstruct the contrast function χ using the measured scattering matrix $\hat{\mathbf{p}}_j^{sct}$. The backward propagation process from the scattered field can be written as:

$$\chi = \mathbf{M}^{\dagger}[\hat{\mathbf{p}}_j^{sct}], \tag{B2}$$

where $\mathbf{M}^{\dagger}[\hat{\mathbf{p}}_j^{sct}] = \sum_{j,\omega}\omega^2[\hat{\mathbf{p}}_j^{inc}(\mathbf{x}')\hat{G}(\mathbf{x}^r-\mathbf{x}')]^*\hat{\mathbf{p}}_j^{sct}(\mathbf{x}^r)$. In the so-called Born inversion, χ can be calculated iteratively by minimizing $E_n = ||\hat{\mathbf{p}}_j^{sct} - \mathbf{M}[\chi_n]||$. This is very similar to iterative ptychography imaging based on the updated object function from the guessed object function, as shown in Eq. (11) in optics.

REFERENCES

[1] Geist, A., "Paving the roadmap to exascale," *SciDAC Review*, Vol. 16, 2010.

[2] Tanter, M. and M. Fink, "Ultrafast imaging in biomedical ultrasound," *IEEE Transactions on Ultrasonics, Ferroelectrics, and Frequency Control*, Vol. 61, No. 1, 102–119, 2014.

[3] Liu, Z., X. Zhang, Y. Mao, Y. Y. Zhu, Z. Yang, C. T. Chan, and P. Sheng, "Locally resonant sonic materials," *Science*, Vol. 289, No. 5485, 1734–1736, 2000.

[4] Fang, N., D. Xi, J. Xu, M. Ambati, W. Srituravanich, C. Sun, and X. Zhang, "Ultrasonic metamaterials with negative modulus," *Nature Materials*, Vol. 5, No. 6, 452–456, 2006.

[5] Ge, H., M. Yang, C. Ma, M.-H. Lu, Y.-F. Chen, N. Fang, and P. Sheng, "Breaking the barriers: Advances in acoustic functional materials," *National Science Review*, Vol. 5, No. 2, 159–182, 2018.

[6] Dong, E., P. Cao, J. Zhang, S. Zhang, N. X. Fang, and Y. Zhang, "Underwater acoustic metamaterials," *National Science Review*, Vol. 10, No. 6, nwac246, 2023.

[7] Torrent, D. and J. Sánchez-Dehesa, "Effective parameters of clusters of cylinders embedded in a nonviscous fluid or gas," *Physical Review B — Condensed Matter and Materials Physics*, Vol. 74, No. 22, 224305, 2006.

[8] Torrent, D., A. Håkansson, F. Cervera, and J. Sánchez-Dehesa, "Homogenization of two-dimensional clusters of rigid rods in air," *Physical Review Letters*, Vol. 96, No. 20, 204302, 2006.

[9] Mei, J., Z. Liu, W. Wen, and P. Sheng, "Effective mass density of fluid-solid composites," *Physical Review Letters*, Vol. 96, No. 2, 024301, 2006.

[10] Wu, Y., Y. Lai, and Z.-Q. Zhang, "Effective medium theory for elastic metamaterials in two dimensions," *Physical Review B — Condensed Matter and Materials Physics*, Vol. 76, No. 20, 205313, 2007.

[11] Fokin, V., M. Ambati, C. Sun, and X. Zhang, "Method for retrieving effective properties of locally resonant acoustic metamaterials," *Physical Review B — Condensed Matter and Materials Physics*, Vol. 76, No. 14, 144302, 2007.

[12] Liu, F., Z. Wang, M. Ke, and Z. Liu, "Metafluids beyond the bulk modulus," *Physical Review Letters*, Vol. 125, No. 18, 185502, 2020.

[13] Sheng, P., J. Mei, Z. Liu, and W. Wen, "Dynamic mass density and acoustic metamaterials," *Physica B: Condensed Matter*, Vol. 394, No. 2, 256–261, 2007.

[14] Zhou, X. and G. Hu, "Analytic model of elastic metamaterials with local resonances," *Physical Review B — Condensed Matter and Materials Physics*, Vol. 79, No. 19, 195109, 2009.

[15] Milton, G. W., *The Theory of Composites*, Cambridge University Press, Cambridge, UK, 2002.

[16] Li, J., L. Fok, X. Yin, G. Bartal, and X. Zhang, "Experimental demonstration of an acoustic magnifying hyperlens," *Nature Materials*, Vol. 8, No. 12, 931–934, 2009.

[17] Berryman, J. G., "Long-wavelength propagation in composite elastic media. I. Spherical inclusions," *The Journal of the Acoustical Society of America*, Vol. 68, No. 6, 1809–1819, 1980.

[18] Mei, J., Z. Liu, W. Wen, and P. Sheng, "Effective dynamic mass density of composites," *Physical Review B — Condensed Matter and Materials Physics*, Vol. 76, No. 13, 134205, 2007.

[19] Krokhin, A. A., J. Arriaga, and L. N. Gumen, "Speed of sound in periodic elastic composites," *Physical Review Letters*, Vol. 91, No. 26, 264302, 2003.

[20] Ingard, U., "On the theory and design of acoustic resonators," *The Journal of the Acoustical Society of America*, Vol. 25, No. 6, 1037–1061, 1953.

[21] Maa, D.-Y., "Potential of microperforated panel absorber," *The Journal of the Acoustical Society of America*, Vol. 104, No. 5, 2861–2866, 1998.

[22] Jin, Y., B. Djafari-Rouhani, and D. Torrent, "Gradient index phononic crystals and metamaterials," *Nanophotonics*, Vol. 8, No. 5, 685–701, 2019.

[23] Hyun, J., W.-H. Cho, C.-S. Park, J. Chang, and M. Kim, "Achromatic acoustic gradient-index phononic crystal lens for broadband focusing," *Applied Physics Letters*, Vol. 116, No. 23, 234102, 2020.

[24] Qu, S., M. Yang, T. Wu, Y. Xu, N. Fang, and S. Chen, "Analytical modeling of acoustic exponential materials and physical mechanism of broadband anti-reflection," *Materials Today Physics*, Vol. 44, 101421, 2024.

[25] Li, J. and C. T. Chan, "Double-negative acoustic metamaterial," *Physical Review E — Statistical, Nonlinear, and Soft Matter Physics*, Vol. 70, No. 5, 055602, 2004.

[26] Ma, G. and P. Sheng, "Acoustic metamaterials: From local resonances to broad horizons," *Science Advances*, Vol. 2, No. 2, e1501595, 2016.

[27] Qu, S. and P. Sheng, "Microwave and acoustic absorption metamaterials," *Physical Review Applied*, Vol. 17, No. 4, 047001, 2022.

[28] Yang, M., G. Ma, Y. Wu, Z. Yang, and P. Sheng, "Homogenization scheme for acoustic metamaterials," *Physical Review B*, Vol. 89, No. 6, 064309, 2014.

[29] Groby, J.-P., M. Malléjac, A. Merkel, V. Romero-García, V. Tournat, D. Torrent, and J. Li, "Analytical modeling of one-dimensional resonant asymmetric and reciprocal acoustic structures as Willis materials," *New Journal of Physics*, Vol. 23, No. 5, 053020, 2021.

[30] Yang, M. and P. Sheng, "Sound absorption structures: From porous media to acoustic metamaterials," *Annual Review of Materials Research*, Vol. 47, 83–114, 2017.

[31] Page, J. H., P. Sheng, H. P. Schriemer, I. Jones, X. Jing, and D. A. Weitz, "Group velocity in strongly scattering media," *Science*, Vol. 271, No. 5249, 634–637, 1996.

[32] Sheng, P. and B. van Tiggelen, *Introduction to Wave Scattering, Localization and Mesoscopic Phenomena*, Springer, 2007.

[33] Hu, H., A. Strybulevych, J. H. Page, S. E. Skipetrov, and B. A. van Tiggelen, "Localization of ultrasound in a three-dimensional elastic network," *Nature Physics*, Vol. 4, No. 12, 945–948, 2008.

[34] Moon, J., Y.-C. Cho, S. Kang, M. Jang, and W. Choi, "Measuring the scattering tensor of a disordered nonlinear medium," *Nature Physics*, Vol. 19, No. 11, 1709–1718, 2023.

[35] Stanton, T. K., D. Chu, J. M. Jech, and J. D. Irish, "New broadband methods for resonance classification and high-resolution imagery of fish with swimbladders using a modified commercial broadband echosounder," *ICES Journal of Marine Science*, Vol. 67, No. 2, 365–378, 2010.

[36] Gu, Z., H. Gao, P.-C. Cao, T. Liu, X.-F. Zhu, and J. Zhu, "Controlling sound in non-Hermitian acoustic systems," *Physical Review Applied*, Vol. 16, No. 5, 057001, 2021.

[37] Adhikari, S., "Damping models for structural vibration," Ph.D. dissertation, University of Cambridge, Cambridge, UK, 2001.

[38] Odonnell, M., E. T. Jaynes, and J. G. Miller, "Kramers-Kronig relationship between ultrasonic attenuation and phase velocity," *The Journal of the Acoustical Society of America*, Vol. 69, No. 3, 696–701, 1981.

[39] Pritz, T., "Unbounded complex modulus of viscoelastic materials and the Kramers-Kronig relations," *Journal of Sound and Vibration*, Vol. 279, No. 3-5, 687–697, 2005.

[40] Guan, F., X. Guo, K. Zeng, S. Zhang, Z. Nie, S. Ma, Q. Dai, J. Pendry, X. Zhang, and S. Zhang, "Overcoming losses in superlenses with synthetic waves of complex frequency," *Science*, Vol. 381, No. 6659, 766–771, 2023.

[41] Kim, S., Y.-G. Peng, S. Yves, and A. Alù, "Loss compensation and superresolution in metamaterials with excitations at complex frequencies," *Physical Review X*, Vol. 13, No. 4, 041024, 2023.

[42] Dong, E., T. Zhang, J. Zhang, X. Su, S. Qu, X. Ye, Z. Gao, C. Gao, J. Hui, Z. Wang, N. X. Fang, and Y. Zhang, "Ultra-broadband transcranial ultrasound by acoustic phase-only hologram with a tungsten metalens," in *2024 Photonics & Electromagnetics Research Symposium (PIERS)*, 1–9, Chengdu, China, 2024.

[43] Shen, C., J. Xu, N. X. Fang, and Y. Jing, "Anisotropic complementary acoustic metamaterial for canceling out aberrating layers," *Physical Review X*, Vol. 4, No. 4, 041033, 2014.

[44] Kruizinga, P., P. van der Meulen, A. Fedjajevs, F. Mastik, G. Springeling, N. de Jong, J. G. Bosch, and G. Leus, "Compressive 3D ultrasound imaging using a single sensor," *Science Advances*, Vol. 3, No. 12, e1701423, 2017.

[45] Gbur, G. and T. D. Visser, *The Structure of Partially Coherent Fields*, 285–341, Elsevier, 2010.

[46] Wolf, E., *Introduction to the Theory of Coherence and Polarization of Light*, Cambridge University Press, 2007.

[47] Born, M. and E. Wolf, *Principles of Optics*, 7th ed., Cambridge University Press, 1999.

[48] Mie, G., "Beiträge zur Optik trüber Medien, speziell kolloidaler Metallösungen," *Annalen der physik*, Vol. 330, No. 3, 377–445, 1908.

[49] Nye, J. F. and M. V. Berry, "Dislocations in wave trains," *Proceedings of the Royal Society of London. A. Mathematical and Physical Sciences*, Vol. 336, No. 1605, 165–190, 1974.

[50] Nye, J. F., *Natural Focusing and Fine Structure of Light: Caustics and Wave Dislocations*, CRC Press, 1999.

[51] Bostan, E., E. Froustey, B. Rappaz, E. Shaffer, D. Sage, and M. Unser, "Phase retrieval by using transport-of-intensity equation and differential interference contrast microscopy," in *2014 IEEE International Conference on Image Processing (ICIP)*, 3939–3943, Paris, France, 2014.

[52] Teague, M. R., "Deterministic phase retrieval: A Green's function solution," *Journal of the Optical Society of America*, Vol. 73, No. 11, 1434–1441, 1983.

[53] Curl, C. L., T. Harris, P. J. Harris, B. E. Allman, C. J. Bellair, A. G. Stewart, and L. M. D. Delbridge, "Quantitative phase microscopy: A new tool for measurement of cell culture growth and confluency in situ," *Pflügers Archiv*, Vol. 448, No. 4, 462–468, 2004.

[54] Beleggia, M., M. A. Schofield, V. V. Volkov, and Y. Zhu, "On the transport of intensity technique for phase retrieval," *Ultramicroscopy*, Vol. 102, No. 1, 37–49, 2004.

[55] Nellist, P. D., B. C. McCallum, and J. M. Rodenburg, "Resolution beyond the 'information limit' in transmission electron microscopy," *Nature*, Vol. 374, No. 6523, 630–632, 1995.

[56] Nellist, P. D. and J. M. Rodenburg, "Electron ptychography. I. Experimental demonstration beyond the conventional resolution limits," *Foundations of Crystallography*, Vol. 54, No. 1, 49–60, 1998.

[57] Rodenburg, J. and A. Maiden, "Ptychography," in *Springer Handbook of Microscopy*, 819–904, Springer, Cham, 2019.

[58] Rodenburg, J. M. and H. M. L. Faulkner, "A phase retrieval algorithm for shifting illumination," *Applied Physics Letters*, Vol. 85, No. 20, 4795–4797, 2004.

[59] Porée, J., D. Posada, A. Hodzic, F. Tournoux, G. Cloutier, and D. Garcia, "High-frame-rate echocardiography using coherent compounding with Doppler-based motion-compensation," *IEEE Transactions on Medical Imaging*, Vol. 35, No. 7, 1647–1657, 2016.

[60] Guizar-Sicairos, M. and J. R. Fienup, "Phase retrieval with transverse translation diversity: A nonlinear optimization approach," *Optics Express*, Vol. 16, No. 10, 7264–7278, 2008.

[61] Wolf, E., "Three-dimensional structure determination of semi-transparent objects from holographic data," *Optics Communications*, Vol. 1, No. 4, 153–156, 1969.

[62] Gusev, V. E. and A. A. Karabutov, "Laser optoacoustics," *NASA STI/Recon Technical Report A*, Vol. 93, 16842, Jul. 1991.

[63] Kim, J., J. Y. Kim, S. Jeon, J. W. Baik, S. H. Cho, and C. Kim, "Super-resolution localization photoacoustic microscopy using intrinsic red blood cells as contrast absorbers," *Light: Science & Applications*, Vol. 8, No. 1, 103, Nov. 2019.

[64] Cao, R., J. Zhao, L. Li, L. Du, Y. Zhang, Y. Luo, L. Jiang, S. Davis, Q. Zhou, A. de la Zerda, and L. V. Wang, "Optical-resolution photoacoustic microscopy with a needle-shaped beam," *Nature Photonics*, Vol. 17, No. 1, 89–95, 2023.

[65] Liu, C., J. Chen, Y. Zhang, J. Zhu, and L. Wang, "Five-wavelength optical-resolution photoacoustic microscopy of blood and lymphatic vessels," *Advanced Photonics*, Vol. 3, No. 1, 016002, 2021.

[66] Liang, Y., L. Jin, B.-O. Guan, and L. Wang, "2 MHz multi-wavelength pulsed laser for functional photoacoustic microscopy," *Optics Letters*, Vol. 42, No. 7, 1452–1455, 2017.

[67] Sun, I.-C., D. S. Dumani, and S. Y. Emelianov, "Applications of the photocatalytic and photoacoustic properties of gold nanorods in contrast-enhanced ultrasound and photoacoustic imaging," *ACS Nano*, Vol. 18, No. 4, 3575–3582, 2024.

[68] Ruiter, N. V., M. Zapf, T. Hopp, and H. Gemmeke, "Ultrasound tomography," in *Quantitative Ultrasound in Soft Tissues*, Vol. 1403, 171–200, Springer, Cham, 2023.

[69] Postema, M., *Fundamentals of Medical Ultrasonics*, CRC Press, 2011.

[70] Lavarello, R. and M. Oelze, "A study on the reconstruction of moderate contrast targets using the distorted Born iterative method," *IEEE Transactions on Ultrasonics, Ferroelectrics, and Frequency Control*, Vol. 55, No. 1, 112–124, 2008.

[71] Archer-Hall, J. A. and D. Gee, "A single integral computer method for axisymmetric transducers with various boundary conditions," *NDT International*, Vol. 13, No. 3, 95–101, 1980.

[72] Hutchins, D. A., H. D. Mair, P. A. Puhach, and A. J. Osei, "Continuous-wave pressure fields of ultrasonic transducers," *The Journal of the Acoustical Society of America*, Vol. 80, No. 1, 1–12, 1986.

[73] Goldstein, A., "Steady state unfocused circular aperture beam patterns in nonattenuating and attenuating fluids," *The Journal of the Acoustical Society of America*, Vol. 115, No. 1, 99–110, 2004.

[74] Douglas Mast, T. and F. Yu, "Simplified expansions for radiation from a baffled circular piston," *The Journal of the Acoustical Society of America*, Vol. 118, No. 6, 3457–3464, 2005.

[75] Marich, K. W., P. S. Green, J. R. Suarez, L. M. Zatz, and A. Macovski, "Real-time imaging with a new ultrasonic camera: Part I, in vitro experimental studies on transmission imaging of biological structures," *Journal of Clinical Ultrasound*, Vol. 3, No. 1, 5–16, 1975.

[76] Schomberg, H., "An improved approach to reconstructive ultrasound tomography," *Journal of Physics D: Applied Physics*, Vol. 11, No. 15, L181–L185, 1978.

[77] Wang, S., P. K. Pandey, G. Lee, R. J. P. van Bergen, L. Sun, Y. Xu, and L. Xiang, "X-ray-induced acoustic computed tomography: 3D X-ray absorption imaging from a single view," *Science Advances*, Vol. 10, No. 49, eads1584, 2024.

[78] Dance, D. R., S. Christofides, A. D. A. Maidment, I. D. McLean, and K. H. Ng, "Diagnostic radiology physics," *International Atomic Energy Agency*, Vol. 299, 12–14, 2014.

[79] Carson, P. L. and T. V. Oughton, "A modeled study for diagnosis of small anechoic masses with ultrasound," *Radiology*, Vol. 122, No. 3, 765–771, 1977.

[80] Glover, G. H. and J. C. Sharp, "Reconstruction of ultrasound propagation speed distributions in soft tissue: Time-of-flight tomography," *IEEE Transactions on Sonics and Ultrasonics*,

Vol. 24, No. 4, 229–234, 1977.

[81] Ozmen, N., R. Dapp, M. Zapf, H. Gemmeke, N. V. Ruiter, and K. W. A. van Dongen, "Comparing different ultrasound imaging methods for breast cancer detection," *IEEE Transactions on Ultrasonics, Ferroelectrics, and Frequency Control*, Vol. 62, No. 4, 637–646, 2015.

[82] Keller, J. B., "Accuracy and validity of the Born and Rytov approximations," *Journal of the Optical Society of America*, Vol. 59, No. 8, 1003–1004, 1969.

[83] Greenleaf, J. F., J. Ylitalo, and J. J. Gisvold, "Ultrasonic computed tomography for breast examination," *IEEE Engineering in Medicine and Biology Magazine*, Vol. 6, No. 4, 27–32, 1987.

[84] André, M. P., H. S. Janée, P. J. Martin, G. P. Otto, B. A. Spivey, and D. A. Palmer, "High-speed data acquisition in a diffraction tomography system employing large-scale toroidal arrays," *International Journal of Imaging Systems and Technology*, Vol. 8, No. 1, 137–147, 1997.

[85] Chenevert, T. L., D. I. Bylski, P. L. Carson, C. R. Meyer, P. H. Bland, D. D. Adler, and R. M. Schmitt, "Ultrasonic computed tomography of the breast. Improvement of image quality by use of cross-correlation time-of-flight and phase-insensitive attenuation measurements," *Radiology*, Vol. 152, No. 1, 155–159, 1984.

[86] Simonetti, F., L. Huang, and N. Duric, "A multiscale approach to diffraction tomography of complex three-dimensional objects," *Applied Physics Letters*, Vol. 95, No. 6, 061904, 2009.

[87] Chew, W. C. and Y. M. Wang, "Reconstruction of two-dimensional permittivity distribution using the distorted Born iterative method," *IEEE Transactions on Medical Imaging*, Vol. 9, No. 2, 218–225, 1990.

[88] Park, E.-Y., X. Cai, J. Foiret, H. Bendjador, D. Hyun, B. Z. Fite, R. Wodnicki, J. J. Dahl, R. D. Boutin, and K. W. Ferrara, "Fast volumetric ultrasound facilitates high-resolution 3D mapping of tissue compartments," *Science Advances*, Vol. 9, No. 22, eadg8176, 2023.

[89] McKeighen, R. E. and M. P. Buchin, "New techniques for dynamically variable electronic delays for real time ultrasonic imaging," in *1977 Ultrasonics Symposium*, 250–254, Phoenix, AZ, USA, 1977.

[90] Mailloux, R. J., "Phased array theory and technology," *Proceedings of the IEEE*, Vol. 70, No. 3, 246–291, 1982.

[91] Friis, H. T. and C. B. Feldman, "A multiple unit steerable antenna for short-wave reception," *Proceedings of the Institute of Radio Engineers*, Vol. 25, No. 7, 841–917, 1937.

[92] Perrot, V., M. Polichetti, F. Varray, and D. Garcia, "So you think you can DAS? A viewpoint on delay-and-sum beamforming," *Ultrasonics*, Vol. 111, 106309, 2021.

[93] Liu, M., Z. Kou, Y. Zhao, J. W. Wiskin, G. J. Czarnota, and M. L. Oelze, "Spectral-based quantitative ultrasound imaging processing techniques: Comparisons of RF versus IQ approaches," *Ultrasonic Imaging*, Vol. 46, No. 2, 75–89, 2024.

[94] Maggioni, M. and T. Berger-Wolf, "Optimization techniques for sparse matrix-vector multiplication on GPUs," *Journal of Parallel and Distributed Computing*, Vol. 93-94, 66–86, 2016.

[95] Gilbert, J. R., C. Moler, and R. Schreiber, "Sparse matrices in MATLAB: Design and implementation," *SIAM Journal on Matrix Analysis and Applications*, Vol. 13, No. 1, 333–356, 1992.

[96] Kou, Z., M. R. Lowerison, Q. You, Y. Wang, P. Song, and M. L. Oelze, "High-resolution power Doppler using null subtraction imaging," *IEEE Transactions on Medical Imaging*, Vol. 43, No. 9, 3060–3071, 2024.

[97] Pinton, G., J.-F. Aubry, E. Bossy, M. Muller, M. Pernot, and M. Tanter, "Attenuation, scattering, and absorption of ultrasound in the skull bone," *Medical Physics*, Vol. 39, No. 1, 299–307, 2012.

[98] Pinton, G. F., G. E. Trahey, and J. J. Dahl, "Sources of image degradation in fundamental and harmonic ultrasound imaging using nonlinear, full-wave simulations," *IEEE Transactions on Ultrasonics, Ferroelectrics, and Frequency Control*, Vol. 58, No. 4, 754–765, 2011.

[99] Menozzi, L. and J. Yao, "Deep tissue photoacoustic imaging with light and sound," *npj Imaging*, Vol. 2, No. 1, 44, 2024.

[100] Ali, R., A. V. Telichko, H. Wang, U. K. Sukumar, J. G. Vilches-Moure, R. Paulmurugan, and J. J. Dahl, "Local sound speed estimation for pulse-echo ultrasound in layered media," *IEEE Transactions on Ultrasonics, Ferroelectrics, and Frequency Control*, Vol. 69, No. 2, 500–511, 2022.

[101] Jaeger, M., G. Held, S. Peeters, S. Preisser, M. Grünig, and M. Frenz, "Computed ultrasound tomography in echo mode for imaging speed of sound using pulse-echo sonography: Proof of principle," *Ultrasound in Medicine & Biology*, Vol. 41, No. 1, 235–250, 2015.

[102] Sanabria, S. J., E. Ozkan, M. Rominger, and O. Goksel, "Spatial domain reconstruction for imaging speed-of-sound with pulse-echo ultrasound: Simulation and in vivo study," *Physics in Medicine & Biology*, Vol. 63, No. 21, 215015, 2018.

[103] Greenleaf, J. F. and R. C. Bahn, "Clinical imaging with transmissive ultrasonic computerized tomography," *IEEE Transactions on Biomedical Engineering*, Vol. 28, No. 2, 177–185, 1981.

[104] Pérez-Liva, M., J. L. Herraiz, J. M. Udías, E. Miller, B. T. Cox, and B. E. Treeby, "Time domain reconstruction of sound speed and attenuation in ultrasound computed tomography using full wave inversion," *The Journal of the Acoustical Society of America*, Vol. 141, No. 3, 1595–1604, 2017.

[105] André, M., J. Wiskin, and D. Borup, "Clinical results with ultrasound computed tomography of the breast," in *Quantitative Ultrasound in Soft Tissues*, 395–432, Springer, 2013.

[106] Jakovljevic, M., S. Hsieh, R. Ali, G. C. L. Kung, D. Hyun, and J. J. Dahl, "Local speed of sound estimation in tissue using pulse-echo ultrasound: Model-based approach," *The Journal of the Acoustical Society of America*, Vol. 144, No. 1, 254–266, 2018.

[107] Bakaric, M., P. Miloro, A. Javaherian, B. T. Cox, B. E. Treeby, and M. D. Brown, "Measurement of the ultrasound attenuation and dispersion in 3D-printed photopolymer materials from 1 to 3.5 MHz," *The Journal of the Acoustical Society of America*, Vol. 150, No. 4, 2798–2805, 2021.

[108] Kuster, G. T. and M. N. Toksoz, "Velocity and attenuation of seismic waves in two-phase media: Part I. Theoretical formulations," *Geophysics*, Vol. 39, No. 5, 587–606, 1974.

[109] Robin, J., J. Robin, A. L. Ber, W. Lambert, M. Fink, and A. Aubry, "Three-dimensional ultrasound matrix imaging," *Nature Communications*, Vol. 14, No. 1, 6793, 2023.

[110] Lambert, W., L. A. Cobus, T. Frappart, M. Fink, and A. Aubry, "Distortion matrix approach for ultrasound imaging of random scattering media," *Proceedings of The National Academy of Sciences*, Vol. 117, No. 26, 14 645–14 656, 2020.

[111] Goodman, J. W., *Statistical Optics*, John Wiley & Sons, 2015.

[112] Goodman, J. W., *Introduction to Fourier Optics*, Roberts and Company Publishers, 2005.

[113] Morgan, M. R., G. E. Trahey, and W. F. Walker, "Multi-covariate imaging of sub-resolution targets," *IEEE Transactions on Medical Imaging*, Vol. 38, No. 7, 1690–1700, 2019.

[114] Mallart, R. and M. Fink, "The van Cittert-Zernike theorem in pulse echo measurements," *The Journal of the Acoustical Soci-*

ety of America, Vol. 90, No. 5, 2718–2727, 1991.
[115] Fink, M., "Time-reversal mirrors," *Journal of Physics D: Applied Physics*, Vol. 26, No. 9, 1333–1350, 1993.
[116] Derode, A., P. Roux, and M. Fink, "Robust acoustic time reversal with high-order multiple scattering," *Physical Review Letters*, Vol. 75, No. 23, 4206, 1995.
[117] Badon, A., V. Barolle, K. Irsch, A. C. Boccara, M. Fink, and A. Aubry, "Distortion matrix concept for deep optical imaging in scattering media," *Science Advances*, Vol. 6, No. 30, eaay7170, 2020.
[118] Song, H. C., W. A. Kuperman, W. S. Hodgkiss, T. Akal, and C. Ferla, "Iterative time reversal in the ocean," *The Journal of the Acoustical Society of America*, Vol. 105, No. 6, 3176–3184, 1999.
[119] Roux, P. and W. A. Kuperman, "Time reversal of ocean noise," *The Journal of the Acoustical Society of America*, Vol. 117, No. 1, 131–136, 2005.
[120] Bourdeloux, C., M. Fink, and F. Lemoult, "Solution to the cocktail party problem: A time-reversal active metasurface for multipoint focusing," *Physical Review Applied*, Vol. 21, No. 5, 054039, 2024.
[121] Fink, M., "Time reversal in acoustics," *Contemporary Physics*, Vol. 37, No. 2, 95–109, 1996.
[122] Clement, G. T. and K. Hynynen, "A non-invasive method for focusing ultrasound through the human skull," *Physics in Medicine & Biology*, Vol. 47, No. 8, 1219–1236, 2002.
[123] Lee, W., P. Croce, R. W. Margolin, A. Cammalleri, K. Yoon, and S.-S. Yoo, "Transcranial focused ultrasound stimulation of motor cortical areas in freely-moving awake rats," *BMC Neuroscience*, Vol. 19, No. 1, 57, 2018.
[124] Huang, X., L. Niu, L. Meng, Z. Lin, W. Zhou, X. Liu, J. Huang, D. Abbott, and H. Zheng, "Transcranial low-intensity pulsed ultrasound stimulation induces neuronal autophagy," *IEEE Transactions on Ultrasonics, Ferroelectrics, and Frequency Control*, Vol. 68, No. 1, 46–53, 2021.
[125] Hu, Z., Y. Yang, L. Yang, Y. Gong, C. Chukwu, D. Ye, Y. Yue, J. Yuan, A. V. Kravitz, and H. Chen, "Airy-beam holographic sonogenetics for advancing neuromodulation precision and flexibility," *Proceedings of the National Academy of Sciences*, Vol. 121, No. 26, e2402200121, 2024.
[126] Maimbourg, G., A. Houdouin, T. Deffieux, M. Tanter, and J.-F. Aubry, "3D-printed adaptive acoustic lens as a disruptive technology for transcranial ultrasound therapy using single-element transducers," *Physics in Medicine & Biology*, Vol. 63, No. 2, 025026, 2018.
[127] Guasch, L., O. C. Agudo, M.-X. Tang, P. Nachev, and M. Warner, "Full-waveform inversion imaging of the human brain," *npj Digital Medicine*, Vol. 3, No. 1, 28, 2020.
[128] Taskin, U., "Full-waveform inversion for breast ultrasound," Ph.D. dissertation, Delft University of Technology, Delft, Netherlands, 2021.
[129] Virieux, J. and S. Operto, "An overview of full-waveform inversion in exploration geophysics," *Geophysics*, Vol. 74, No. 6, WCC1–WCC26, 2009.
[130] Muller, M., J.-L. Gennisson, T. Deffieux, M. Tanter, and M. Fink, "Quantitative viscoelasticity mapping of human liver using supersonic shear imaging: Preliminary in vivo feasability study," *Ultrasound in Medicine & Biology*, Vol. 35, No. 2, 219–229, 2009.
[131] Muller, M., A. Sutin, R. Guyer, M. Talmant, P. Laugier, and P. A. Johnson, "Nonlinear resonant ultrasound spectroscopy (NRUS) applied to damage assessment in bone," *The Journal of the Acoustical Society of America*, Vol. 118, No. 6, 3946–3952, 2005.
[132] Zhou, J., Y. Guo, Q. Sun, F. Lin, C. Jiang, K. Xu, and D. Ta, "Transcranial ultrafast ultrasound Doppler imaging: A phantom study," *Ultrasonics*, Vol. 144, 107430, 2024.
[133] Tanter, M., J.-L. Thomas, and M. Fink, "Focusing and steering through absorbing and aberrating layers: Application to ultrasonic propagation through the skull," *The Journal of the Acoustical Society of America*, Vol. 103, No. 5, 2403–2410, 1998.
[134] Jiménez-Gambín, S., N. Jiménez, A. N. Pouliopoulos, J. M. Benlloch, E. E. Konofagou, and F. Camarena, "Acoustic holograms for bilateral blood-brain barrier opening in a mouse model," *IEEE Transactions on Biomedical Engineering*, Vol. 69, No. 4, 1359–1368, 2022.
[135] Chen, H. and C. T. Chan, "Acoustic cloaking in three dimensions using acoustic metamaterials," *Applied Physics Letters*, Vol. 91, No. 18, 183518, 2007.
[136] Li, L., Y. Diao, H. Wu, and W. Jiang, "Complementary acoustic metamaterial for penetrating aberration layers," *ACS Applied Materials & Interfaces*, Vol. 14, No. 25, 28 604–28 614, 2022.
[137] Park, C. I., S. Choe, W. Lee, W. Choi, M. Kim, H. M. Seung, and Y. Y. Kim, "Ultrasonic barrier-through imaging by Fabry-Perot resonance-tailoring panel," *Nature Communications*, Vol. 14, No. 1, 7818, 2023.
[138] Hertzberg, Y. and G. Navon, "Bypassing absorbing objects in focused ultrasound using computer generated holographic technique," *Medical Physics*, Vol. 38, No. 12, 6407–6415, 2011.
[139] Melde, K., A. G. Mark, T. Qiu, and P. Fischer, "Holograms for acoustics," *Nature*, Vol. 537, No. 7621, 518–522, 2016.
[140] Zhu, Y., J. Hu, X. Fan, J. Yang, B. Liang, X. Zhu, and J. Cheng, "Fine manipulation of sound via lossy metamaterials with independent and arbitrary reflection amplitude and phase," *Nature Communications*, Vol. 9, No. 1, 1632, 2018.
[141] Lu, J.-Y., H. Zou, and J. F. Greenleaf, "Biomedical ultrasound beam forming," *Ultrasound in Medicine & Biology*, Vol. 20, No. 5, 403–428, 1994.
[142] Lu, J.-Y., "2D and 3D high frame rate imaging with limited diffraction beams," *IEEE Transactions on Ultrasonics, Ferroelectrics, and Frequency Control*, Vol. 44, No. 4, 839–856, 1997.
[143] Jiménez-Gambín, S., N. Jiménez, J. M. Benlloch, and F. Camarena, "Generating Bessel beams with broad depth-of-field by using phase-only acoustic holograms," *Scientific Reports*, Vol. 9, No. 1, 20104, 2019.
[144] Leedom, D. A., R. Krimholtz, and G. L. Matthaei, "Equivalent circuits for transducers having arbitrary even- or odd-symmetry piezoelectric excitation," *IEEE Transactions on Sonics and Ultrasonics*, Vol. 18, No. 3, 128–141, 1971.
[145] Fink, M. and M. Tanter, "Multiwave imaging and super resolution," *Physics Today*, Vol. 63, No. 2, 28–33, 2010.
[146] Mason, W. P., *Electromechanical Transducers and Wave Filters*, 2nd ed., D. Van Nostrand Co., Inc., New York, 1948.
[147] Mason, W. P. and R. B. Lindsay, "Physical acoustics and the properties of solids," *Physics Today*, Vol. 12, No. 4, 34–34, 1959.
[148] Redwood, M., "Transient performance of a piezoelectric transducer," *The Journal of the Acoustical Society of America*, Vol. 33, No. 4, 527–536, 1961.
[149] Krimholtz, R., D. A. Leedom, and G. L. Matthaei, "New equivalent circuits for elementary piezoelectric transducers," *Electronics Letters*, Vol. 6, No. 13, 398–399, 1970.
[150] Sherrit, S., S. P. Leary, B. P. Dolgin, and Y. Bar-Cohen, "Comparison of the Mason and KLM equivalent circuits for piezoelectric resonators in the thickness mode," in *1999 IEEE Ul-*

trasonics Symposium. Proceedings. International Symposium (Cat. No.99CH37027), Vol. 2, 921–926, Tahoe, NV, USA, 1999.

[151] Delannoy, B., R. Torguet, C. Bruneel, E. Bridoux, J. M. Rouvaen, and H. Lasota, "Acoustical image reconstruction in parallel-processing analog electronic systems," *Journal of Applied Physics*, Vol. 50, No. 5, 3153–3159, 1979.

[152] Delannoy, B., R. Torguet, C. Bruneel, and E. Bridoux, "Ultrafast electronical image reconstruction device," in *Echocardiology*, 447–450, Springer, Dordrecht, 1979.

[153] Sandrin, L., S. Catheline, M. Tanter, and M. Fink, "2D transient elastography," in *Acoustical Imaging*, 485–492, Springer, Boston, 2002.

[154] Sandrin, L., M. Tanter, S. Catheline, and M. Fink, "Shear modulus imaging with 2-D transient elastography," *IEEE Transactions on Ultrasonics, Ferroelectrics, and Frequency Control*, Vol. 49, No. 4, 426–435, 2002.

[155] Montaldo, G., M. Tanter, J. Bercoff, N. Benech, and M. Fink, "Coherent plane-wave compounding for very high frame rate ultrasonography and transient elastography," *IEEE Transactions on Ultrasonics, Ferroelectrics, and Frequency Control*, Vol. 56, No. 3, 489–506, 2009.

[156] Lee, W.-N., M. Pernot, M. Couade, E. Messas, P. Bruneval, A. Bel, A. A. Hagege, M. Fink, and M. Tanter, "Mapping myocardial fiber orientation using echocardiography-based shear wave imaging," *IEEE Transactions on Medical Imaging*, Vol. 31, No. 3, 554–562, 2012.

[157] Lu, J.-Y. and J. F. Greenleaf, "Pulse-echo imaging using a nondiffracting beam transducer," *Ultrasound in Medicine & Biology*, Vol. 17, No. 3, 265–281, 1991.

[158] Lu, J.-Y. and J. F. Greenleaf, "Ultrasonic nondiffracting transducer for medical imaging," *IEEE Transactions on Ultrasonics, Ferroelectrics, and Frequency Control*, Vol. 37, No. 5, 438–447, 1990.

[159] Lu, J.-Y. and J. F. Greenleaf, "Experimental verification of nondiffracting X waves," *IEEE Transactions on Ultrasonics, Ferroelectrics, and Frequency Control*, Vol. 39, No. 3, 441–446, 1992.

[160] Durnin, J., J. J. Miceli Jr., and J. H. Eberly, "Diffraction-free beams," *Physical Review Letters*, Vol. 58, No. 15, 1499, 1987.

[161] Durnin, J., "Exact solutions for nondiffracting beams. I. The scalar theory," *Journal of the Optical Society of America A*, Vol. 4, No. 4, 651–654, 1987.

[162] Gabor, D., "A new microscopic principle," *Nature*, Vol. 161, 777–778, 1948.

[163] Leith, E. N. and J. Upatnieks, "Wavefront reconstruction with diffused illumination and three-dimensional objects," *Journal of the Optical Society of America*, Vol. 54, No. 11, 1295–1301, 1964.

[164] Denisyuk, Y. N., "Photographic reconstruction of the optical properties of an object in its own scattered radiation field," *Soviet Physics Doklady*, Vol. 7, 543, 1962.

[165] Benton, S. A., "Hologram reconstruction with extended incoherent sources," *Journal of the Optical Society of America A*, Vol. 59, 1545, 1969.

[166] Goodman, J. W., "Digital image formation from electronically detected holograms," *Computerized Imaging Techniques*, Vol. 10, 176–181, 1967.

[167] Lohmann, A. W. and D. P. Paris, "Binary Fraunhofer holograms, generated by computer," *Applied Optics*, Vol. 6, No. 10, 1739–1748, 1967.

[168] Wiley, C. A., "Synthetic aperture radars," *IEEE Transactions on Aerospace and Electronic Systems*, No. 3, 440–443, 2007.

[169] De Marchi, L., "The blossoming of ultrasonic metatransducers," *IEEE Transactions on Ultrasonics, Ferroelectrics, and Frequency Control*, Vol. 71, No. 9, 1097–1105, 2024.

[170] Brown, M. D., B. S. Generowicz, S. Dijkhuizen, S. K. E. Koekkoek, C. Strydis, J. G. Bosch, P. Arvanitis, G. Springeling, G. J. T. Leus, C. I. De Zeeuw, *et al.*, "Four-dimensional computational ultrasound imaging of brain hemodynamics," *Science Advances*, Vol. 10, No. 3, eadk7957, 2024.

[171] Fisher, R. A., "On the mathematical foundations of theoretical statistics," *Philosophical Transactions of the Royal Society of London, Series A: Containing Papers of a Mathematical or Physical Character*, Vol. 222, No. 594-604, 309–368, 1922.

[172] Dong, E., Z. Song, Y. Zhang, S. G. Mosanenzadeh, Q. He, X. Zhao, and N. X. Fang, "Bioinspired metagel with broadband tunable impedance matching," *Science Advances*, Vol. 6, No. 44, eabb3641, 2020.

[173] Soumekh, M., *Synthetic Aperture Radar Signal Processing*, Wiley, New York, 1999.

[174] Mamou, J. and M. L. Oelze, *Quantitative Ultrasound in Soft Tissues*, Springer, 2013.

[175] Franceschini, E., F. T. H. Yu, F. Destrempes, and G. Cloutier, "In vivo ultrasound characterization of red blood cell aggregation using the structure factor size and attenuation estimator," in *2009 IEEE International Ultrasonics Symposium*, 301–304, Rome, Italy, 2009.

[176] Dally, W. J., S. W. Keckler, and D. B. Kirk, "Evolution of the graphics processing unit (GPU)," *IEEE Micro*, Vol. 41, No. 6, 42–51, 2021.

[177] Craig, S. R., P. J. Welch, and C. Shi, "Non-Hermitian complementary acoustic metamaterials for lossy barriers," *Applied Physics Letters*, Vol. 115, No. 5, 051903, 2019.

[178] Panagakos, F. and F. Scannapieco, "Periodontal inflammation: From gingivitis to systemic disease," *Gingival Diseases: Their Aetiology, Prevention and Treatment*, 155–168, 2011.

[179] Park, T. H., "Evaluation of carotid plaque using ultrasound imaging," *Journal of Cardiovascular Ultrasound*, Vol. 24, No. 2, 91–95, 2016.

[180] Tanter, M., J. Bercoff, L. Sandrin, and M. Fink, "Ultrafast compound imaging for 2-D motion vector estimation: Application to transient elastography," *IEEE Transactions on Ultrasonics, Ferroelectrics, and Frequency Control*, Vol. 49, No. 10, 1363–1374, 2002.

[181] Jahng, G.-H., S. Park, C.-W. Ryu, and Z.-H. Cho, "Magnetic resonance imaging: Historical overview, technical developments, and clinical applications," *Progress in Medical Physics*, Vol. 31, No. 3, 35–53, 2020.

[182] Li, J., T. Su, B. Zhao, F. Lv, Q. Wang, N. Navab, Y. Hu, and Z. Jiang, "Ultrasound report generation with cross-modality feature alignment via unsupervised guidance," *IEEE Transactions on Medical Imaging*, Vol. 44, No. 1, 19–30, 2025.

[183] Needham, L.-M., C. Saavedra, J. K. Rasch, D. Sole-Barber, B. S. Schweitzer, A. J. Fairhall, C. H. Vollbrecht, S. Wan, Y. Podorova, A. J. Bergsten, *et al.*, "Label-free detection and profiling of individual solution-phase molecules," *Nature*, Vol. 629, No. 8014, 1062–1068, 2024.

[184] Selmke, M. and F. Cichos, "Photothermal single particle Rutherford scattering microscopy," *Physical Review Letters*, Vol. 110, No. 10, 103901, 2013.

[185] Cheng, Z. and L. V. Wang, "Focusing light into scattering media with ultrasound-induced field perturbation," *Light: Science & Applications*, Vol. 10, No. 1, 159, 2021.

[186] Alles, E. J., S. Noimark, E. Maneas, E. Z. Zhang, I. P. Parkin, P. C. Beard, and A. E. Desjardins, "Video-rate all-optical ul-

trasound imaging," *Biomedical Optics Express*, Vol. 9, No. 8, 3481–3494, 2018.

[187] Lewis-Thompson, I., E. Z. Zhang, P. C. Beard, A. E. Desjardins, and R. J. Colchester, "All-optical ultrasound catheter for rapid B-mode oesophageal imaging," *Biomedical Optics Express*, Vol. 14, No. 8, 4052–4064, 2023.

[188] Wang, L., Y. Zhao, B. Zheng, Y. Huo, Y. Fan, D. Ma, Y. Gu, and P. Wang, "Ultrawide-bandwidth high-resolution all-optical intravascular ultrasound using miniaturized photoacoustic transducer," *Science Advances*, Vol. 9, No. 23, eadg8600, 2023.

[189] Deng, X., W. Tao, Y. Diao, B. Sang, and W. Sha, "Imaging analysis of photonic integrated interference imaging system based on compact sampling lenslet array considering on-chip optical loss," *Photonics*, Vol. 10, No. 7, 797, 2023.

[190] Liu, G., D. Wen, W. Fan, Z. Song, B. Li, and T. Jiang, "Single photonic integrated circuit imaging system with a 2D lens array arrangement," *Optics Express*, Vol. 30, No. 4, 4905–4918, Feb. 2022.